POLITEHNICA UNIVERSITY OF BUCHAREST

FACULTY OF CHEMICAL ENGINEERING AND BIOTECHNOLOGIES

BONE GRAFTING MATERIALS FOR DENTISTRY

PhD Thesis Summary

PhD Supervisor,

Prof. Dr. Ing. Ecaterina Andronescu

PhD student,

Ing. Cristina Rodica Dumitrescu

Bucureşti,

2022

PhD Thesis contains:

Pages : 192

Figures: 93

Tables : 33

References : 247

Key words: Bone grafting bio-composite, mesoporous nano-powder of hydroxyapatite, sodium-potassium niobate powders, chitosan, lyophilization method, hydrothermal microwave assisted ripening, bone augmentation

CONTENT

INTRODUCTION

From statistical studies published in 2022, the total costs involved in the treatment of periodontal disease cases reported in 2018 in the US was estimated at USD 3.49 billion and EUR 2.52 billion in Europe[1]. It is estimated that approximately 10% of the world's population is severely affected by periodontitis, the delay and failure treatments leads to tooth loss [2]. In addition to periodontal diseases, other deficiencies can lead to tooth loss, including the degeneration of bone tissue caused by age and sex. Recent studies have shown the connection between the occurrence of periodontal diseases in women 0-4 years after the onset of menopause [3]. The first goal in periodontal tissue engineering is the regeneration of the supporting tissue of the teeth [2]. Bone deficiency of the jaws is often attributed to accidents, surgical removal of benign lesions or malignant neoplasms, congenital anomalies, periodontal inflammation, abscess or tooth extraction, and finally jaw atrophy due to advanced age or general illness[2, 4-13]. These bone defects require rehabilitation for several reasons, e.g. maintaining the normal anatomical contour, eliminating the empty space, aesthetic restoration, placement of dental implants and above all preventing the physiological process of bone resorption [2, 5-13].

Tissues such as bone, cartilage, dentin, tendons have demonstrated piezoelectric properties. In 1960, Fukada observed that mechanical tension induces a piezoelectric effect in bone determined by the sliding of collagen fibers against each other[14]. The piezoelectric effect is characterized by a linear transformation between mechanical and electrical variables. In general, piezoelectric materials can generate different electrical charges on opposite surfaces in response to mechanical stress, such as stretching, compression, or tilting [15]. Hard connective tissues dynamically remodel for their functional requirements by chemical signals transmitted by cells or the extracellular matrix and electrical signals by synapses or by the piezoelectric effect. The hard connective tissue contains organic and inorganic constituents: collagenous or non-collagenous proteins that give flexibility to the bone tissue as well as the cellular component that ensures the physiological functioning of the tissue; the mineral component and water have both functional and structural roles. The latest generation bone grafting biomaterials attempt to mimic the composition and structure of bone tissue, down to the organic constituents that can induce rejection effects from the host body. Hydroxyapatite is the majority mineral component of bone. Also called biological apatite, this mineral, which constitutes the mechanical support of bone tissue, has specific morpho-structural characteristics: the nanometric polycrystalline particles of biological apatite, with platelet and rod morphology, are packed into three-dimensional structures with helical structure of type I collagen fibers, this composite inducing all important functional tissue particularities during osteogenesis as well as in reparative processes. A biomaterial implanted as a bone addition and substitution material must respond to several important challenges, which will decide the success of the grafting operation [16]: biocompatibility with the biological environment translated by the moderate intensity of inflammatory processes and macrophage phagocytosis activity as the body's response to the presence of the implant [17]; the bioactivity or inert behavior of biomaterials must be in accordance with physiological biochemical processes and the preservation of some functional properties (for example, mechanical resistance) ; the stimulation of osteoinductive processes, i.e. the ability of the material to achieve bonds and interactions that synergistically lead to the activation of

osteoblasts in *de novo* bone generation processes [18, 19] ; induction of hemostatic effects, as appropriate, which favor the activity of chondrocytes, macrophages, platelets [20, 21]; to have antibacterial properties that allow the reduction of the bacterial population or even interrupt the bacterial replication [22].

Different techniques such as changing the chemistry, composition or designing the surface structure of biomaterials (micro or nanoparticulate), external application of electrical stimuli and polarization or magnetic field can improve the antibacterial response, adhesiveness but especially the osteoinductive response [23]. The adhesion of bacteria to the surface of the biomaterial (implant) takes place through electrostatic interactions but also through van der Waals bonds, on hydrophobic surfaces. Usually, the outer membrane of bacteria is charged with negative charges (more strongly negative in gram-negative than gram-positive germs) due to the ionization of the active hydrogen of the functional groups (carbonyl, phosphate, amino and hydroxyl). Antibacterial agents target the cell genome, respiration, division, metabolic pathway and membrane disruption of bacterial cells to kill them [22]. Forming self-protective bio-films, the most common cocci in implant-associated infections are: staphylococci gram-positive (*Staphylococcus aureus*, *Listeria monocytogenes , etc.*), *streptococcus* and *enterococcus*, and gram-negative aerobic species include enterobacteria (*Salmonella enteritidis*, *E. coli* și *Pseudomonas aerugenosa)* [23].

The PhD thesis was structured in two parts: Part I "Critical study of literature data" which includes chapter 1 and 2; Part II of "Original Contributions" comprising chapters 3, 4 and 5.

PART I CRITICAL STUDY OF LITERATURE

CHAPTER 1 ANATOMY AND PHYSIOLOGY OF BONE TISSUE, FIZIOLOGYCAL MECHANISMS FOR BONE REPAIR

Chapter 1 presents general information about the anatomy and physiology of bone tissue, which has a high capacity for self-healing in case of cracks, dental extractions or fractures, if they do not exceed certain limits. The composition, structure and morphology of bone tissue is important to know in the context of the study of grafts of additional materials, as it differs depending on the type of bone and the functional properties to which it must respond physiologically. Also, in chapter 1, notions about the physiology of bone tissue were provided, which are in correlation with its structure, composition and morphology. There are two types of bone tissue in the oral cavity: the upper and lower jawbones and the teeth. The jawbones have the ability to self-repair as an adaptation to the physiological function of mastication and support, while the teeth do not. This different behavior of the two types of bone tissue is supported structurally and compositionally differently: the jawbones, although structurally dense for resistance to mechanical stress, contain an area of spongy tissue that allows better vascularization and innervation, rich in cells that can differentiate and specializes in bone synthesis; the teeth, although also structured in several layers, are compositionally richer in minerals, with a role of mechanical and

chemical resistance, than the organic mass that gives elasticity, but they have a reduced content in odontoblasts even in the dentinal layers richer in canicular pores from the proximity of the dental pulp.

The mechanisms and stages of the formation of different types of bone tissue as well as the restoration of bone defects were also presented in Chapter 1, being necessary to know the three, according to some authors, 4 phases: inflammatory, repair and the final remodeling phase [18, 19, 24].

- ✓ The piezoelectric effect that manifests itself in the body in the ossification processes can involve several sub-processes:
  - The application of mechanical stresses to the bone tissue of the dental alveoli causes the structural proteins (collagen, proteoglycans, etc.) to deform and self-induce an electrical surface charge with the role of:
    - signaling on the membrane of osteoblast cells in the bone matrix, activating them.
    - surface functional groups polarizing lead to increasing the electrical potential and mineralization capacity, thus bone restoration;
    - surface polarization increases cellular and protein adhesion by manifesting electrostatic attraction effects.

The use of biomaterial grafts with piezoelectric properties can potentiate both the osteopromoting effect and can act as a weak antibacterial agent, according to the mechanisms described in this chapter.

CHAPTER 2 BONE GRAFTING BIOMATERIALS FOR DENTISTRY

In Chapter 2, were presented the reasons why bone augmentation interventions are needed using additional materials in the dental field. Also, was made an overview of the characteristics that biomaterials must fulfill in order to generate improvements in bone augmentation results. In the last part of Chapter 2, the categories of bone addition materials used in the dental field were presented in detail.

Dental extractions are the main cause of bone loss in the dental field. Following them, on the one hand, part of the connective tissue and bone tissue is removed, but the phenomenon of physiological bone resorption occurs, caused by the loss of vascularization and innervation, as well as functional support characteristics. In most cases, the restoration of the dental alveoli following tooth extractions, without exogenous interventions, involves the formation of fibrous tissue, with little vascularity, which does not represent a suitable support for the dental implant. Clinical studies have shown that important for the success of the grafting operation is the form of presentation of the materials: of the newest generation are the addition materials in the form of gel, which present a better bioactivity and the injection technique creates minimal discomfort for the patient. Scaffold-type grafts must present a high porosity that confers a good adhesion of the growth proteins, high mechanical resistance is not an requirement,

low potential inflammatory effect inducing, additionally a slight hemostatic effect, biodegradable and moderately chemically active, and osteopromoting electrical signaling.

The alternative of synthetic bone addition materials used is still considered unsafe by dental clinicians, the proof being their "classic" variants compared to the current state of research, approved for use in the dental field. The studies of recent years on alloplastic bone addition materials aimed at the creation of materials that, in addition to structural and compositional mimicry, induce properties with positive effects on processes complementary to ossification, such as: improving the adhesion of specific proteins, angiogenesis, bio signaling, polarization, bacteriostatic and antifungal effect, hemostasis or hemolysis, etc.

A new approach in dental practice is the impregnation of alloplastic materials with the serum extracted from the patient's blood, the technique that significantly improves the acceptance of the graft by the body and widens the ability to use the many variants of synthetic bone addition materials.

THE RESEARCH STUDY MOTIVATIONS

The research theme aims at the synthesis of a biocomposite that is compositionally mimetic with the bone tissue in order to preserve some essential properties, but which contains a component with piezoelectric properties and without cytotoxic effects that, once implanted in the alveolar bone defect, can potentiate through polarization: signaling, the formation reactions kinetics improvement as well as the adhesion of cells or biopolymers from the bone extracellular matrix. Properties such as biocompatibility translated by the possibility of inducing a moderate inflammatory effect, stimulation of cell adhesion or source of biopolymers and minerals were provided by the manometric powder of hydroxyapatite from biogenic sources (HA) and chitosan with low molecular weight and medium degree of deacetylation (CSL). The piezoelectric materials such as the solid solution of sodium and potassium niobate (KNN) is an extremely current research field, in the context of enhancing necessity of health security and environmental protection, but also due to the use in electronic fields and last generation medical applications (biosensors, medical devices for generating ultrasound and high-frequency energy, sonar, etc.). Moreover, the polarization effect of the bio-material granules in the HA-KNN-CSL system can induce micro-electric fields useful in bio-signaling, antibacterial and antifungal mechanisms and the increase of cellular or molecular adhesion through electrostatic attraction as well as the modification of the membrane potential cell phones. Also, the bone addition biomaterials used in dentistry must meet complex requirements and induce antibacterial effects, reducing the inflammatory or even hemostatic reaction, as well as being as versatile as possible in terms of shaping or putting into operation in dental offices.

THE RESEARCH STUDY OBJECTIVES

The general objective of the research study within the PhD thesis is the synthesis of a bio-composite in the HA-KNN-CSL system that would sum up the functional properties of a state-of-the-art bone addition material, easy to graft for alveolar bone augmentation.

The specific objectives of the research study were summarized in three directions:

- The use of some synthesis methods such as the microwave-assisted hydrothermal method (HTMW) or the lyophilization drying method, which generate traceable and predictable results by controlling process parameters or raw materials.
- The composite components synthesis in the HA-KNN-CSL system were managed in order to gain the right characteristics: mesoporous nanometric powder of carbonated apatite containing trace elements, chitosan hydrogel with antibacterial, coagulant and anti-inflammatory action, as well as the sub-micron powder of niobate solid solution of sodium and potassium, containing crystals with orthorhombic and tetragonal symmetry at the limit of the morphotropic phase ($K_{0.5}Na_{0.5}NbO_3$), with the best piezoelectric coefficient d33;
- Synthesis of the bio-composite in the HA-KNN-CSL system having the right proportions of the components, so as to ensure the best piezoelectric properties, moderate bioactivity, antibacterial and antifungal properties but under the conditions of a minimal cytotoxic effect and a good cellular activity.

PART II ORIGINAL CONTRIBUTIONS

CAPITOLUL 3 HYDROXYAPATITE POWDERS: SYNTHESIS FROM EGGSHELL SOURCE AND COMPOSITIONAL AND MORPHOSTRUCTURAL CHARACTERISATION

The synthesis method of the first biocomposite component is detailed in Chapter 3. The precursors, the reaction conditions and the technological parameters of the hydrothermal maturation method using microwaves as the heating source of the system are presented. Also, an extensive characterization of both the raw materials (eggshell) and, comparatively, of the 5 obtained hydroxyapatite specimens is carried out. In the second part of Chapter 3, are presented a comparative compositional and morpho-structural properties of the synthesized carbonate apatite specimen HA1 *versus* two trademark xenografts Bio-Oss® and Gen-OS® which are used with good results in current dental practice.

The microwave assisted hydrothermal method was adopted for the synthesis of carbonated hydroxyapatite starting from a natural and cheap source which is eggshell. Eggshell is a source of calcite (96%) and the option of using it as a calcite precursor after calcination was chosen, the obtained calcium oxide was precipitated to hydroxyapatite by adding dibasic ammonium acid phosphate, titrated at a rate of 2 mL/minute, under continuous magnetic homogenization, with the secondary reaction product (ammonium hydroxide) acting as a pH corrector in the strongly basic range. The maturation of the precipitate was followed in two directions: by hydrothermal treatment and classical maturation at room temperature for a duration of 12 h and 48 h (samples named HA_CP_12, HA_CP_48). Microwave-assisted hydrothermal ripening (HTMW) was also pursued in two variants: hydrothermal treatment at high temperature (200°C) with a full cycle duration of 60 minutes (HA1) and a reduced duration of 30

minutes at 135° C, which were later matured under normal conditions for 12 and 48 hours respectively (HA_HT_12, HA_HT_48).

Following the compositional, morpho-structural and cytotoxic characterization, the following conclusions could be issued:

- Absorbance IR spectra (FTIR) showed the presence of B-type carbonate groups, with a higher content in the classically matured samples, a weak or absent vibration of the H-O bond and a high similarity of the FTIR spectra of both profiles and amplitudes of the spectra for all samples, so at the very good compositional similarity with carbonate apatite (Figure 1); the content of type A carbonate groups substituting the PO43- groups in the C/P hydroxyapatite network determined with the empirical equation [25], it falls between 0.0304 – 0.0737, the highest value of this ratio being found at HA_CP_12.

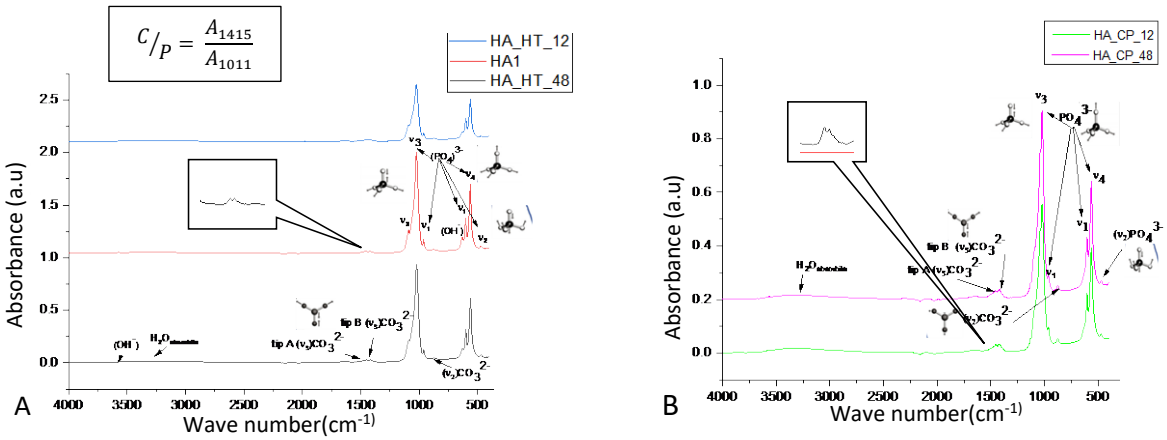

Figure 1 Comparative FTIR absorption spectra for: A) HTMW maturated samples HA1 and HA_HT_12, HA_HT_48; B) classical maturated samples at room temperature HA_CP_12, HA_CP_48

- The XRF spectra highlight the preservation of trace elements (Na, Mg, K, Sr, Si, Fe, Cl, etc.) in proportions greater than half of the eggshell content in all synthesized samples, but also Ca/P ratios < 2 (~1.8) for hydrothermally synthesized samples and Ca/P >2 for classic ripening.
- X-ray diffraction analysis and Rietveld structural refinement highlighted the unique hydroxyapatite phase where the peak profiles differ slightly in amplitude and width (Figure 2), with variable content of hexagonal phases and a monoclinic phase, the majority in the samples obtained by hydrothermal maturation; the monoclinic phase kept the other lattice parameters as in the case of hexagonal symmetry, deriving from the hexagonal phase by distorting the angle of the base plane from 120° by ± 0.5° and elongating according to the parameter b of the crystalline lattice (); the hydrothermally treated samples had the highest degree of crystallinity, and of these, HA1 showed crystallinity of ~90%;

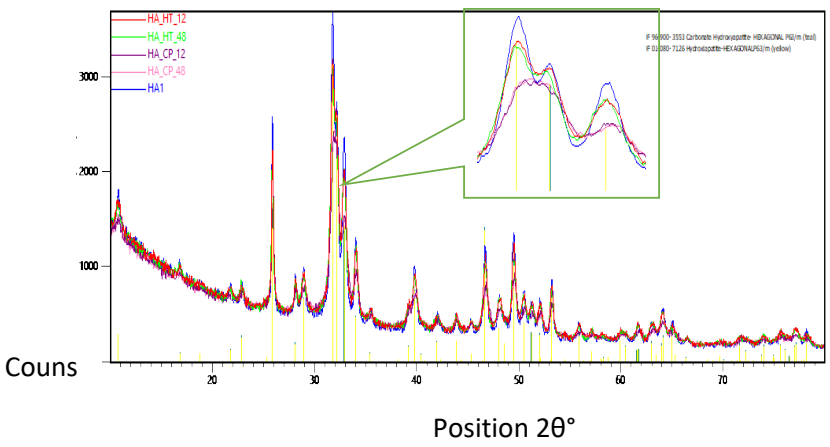

Figure 2 Overlapped X-Ray diffraction patterns for samples HA_HT_12, HA_HT_48, HA1, HA_CP_12 and HA_CP_48

- The SEM micrographs showed the similarity between the loose, fluffy texture of the particle aggregates, with sizes as small as 1 µm, the difficulty to measure the particle size even at 100,000x magnifications; EDS confirms Ca/P<2 for hydrothermally matured samples.
- From the analysis of the TEM, HRTEM and SAED images, it was highlighted that the morphology of the polycrystalline particles of nanometric sizes is different: the hydrothermally treated samples have the morphology of mesoporous nano-bars, and the classically matured ones are prismatic plates, having a porosity placed at the upper limit of microporosity (Figure 3);

Table 1 Phases proportion structure and unit cell parameters determined by Rietveld refinement method using diffraction patterns PDF 04-016-1185 (M P21/b) and PDF 01-080-7126 (H P63/m) for the samples HA_CP_12, HA_CP_48, HA_HT_12, HA_HT_48 and HA1.

Sample	HA M, P21/b Z=4 PDF 01-089-4405	HA H P63/m Z=2 PDF 04-080-7126	HA_CP_12		HA_CP_48		HA_HT_12		HA_HT_48		HA1	
Unit cell parameters			M 23.5 %	H 76.4 %	M 17.7 %	H 82.3 %	M 94 %	H 6 %	M 97 %	H 3 %	M 96.9 %	H 3.1 %
a (Å)	9.426	9.460	9.617	9.417	9.671	9.408	9.456	9.631	9.432	9.304	9.408	9.167
b(Å)	18.856	9.460	19.231	9.417	19.257	9.408	18.864	9.631	18.852	9.304	18.943	9.167
c(Å)	6.887	6.885	6.881	6.884	6.883	6.885	6.885	6.885	6.884	6.880	6.886	6.902
V(Å³)	1060.4	539.4	1084.7	528.7	1048.8	527.8	1060.2	550.7	1057.8	515.8	1062.7	503.2
α(⁰)	90	90	90	90	90	90	90	90	90	90	90	90
β(⁰)	90	90	90	90	90	90	90	90	90	90	90	90
Υ(⁰)	119.9	120	120.5	120	120.8	120	120.31	120	120.2	120	120.02	120
Average crystallites sizes (nm)	-	-	33.8642		35.6023		31.9256		32.6276		31.98	
Standard deviation (nm)	-	-	19.36687		19.52428		9.53257		9.59872		1.89	
Micro-strains(%)	-	-	0.67935		0.6766		0.63205		0.5142		0.5208	
Cystallinity (%)	-	-	33.95		36.61		60.46		72.44		84.20	

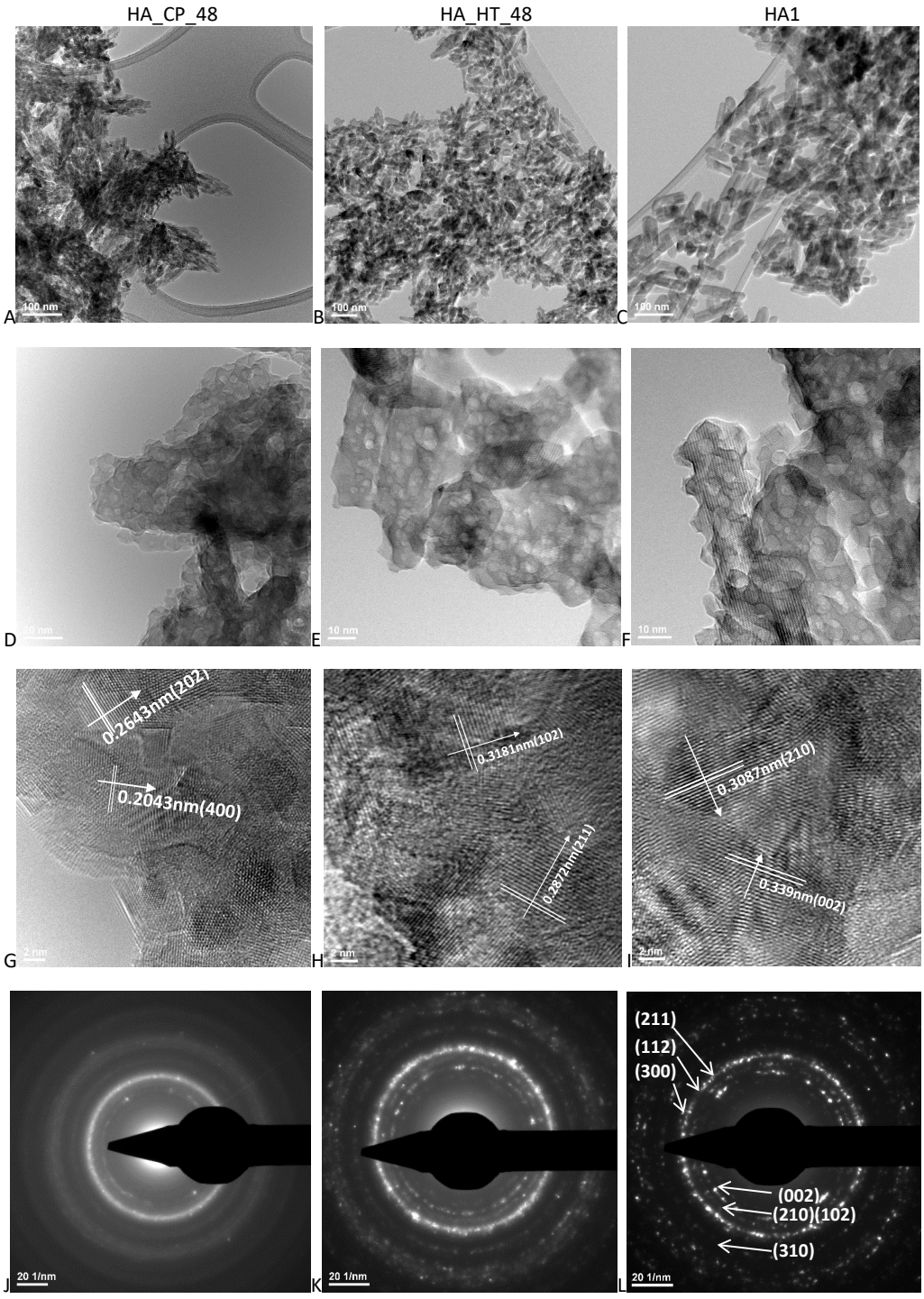

Figure 3 Micrographic TEM (A-F) for samples HA_CP_48 (A, D), HA_HT_48 (B, E), HA1 (C, F); HR-TEM Images for HA_CP_48 (G), HA_HT_48 (H), HA1 (I) samples ; SAED Images for HA_CP_48 (J), HA_HT_48 (K), HA1 (L) samples.

- The cytotoxic behavior of the powders against the mouse osteoblast cell cultures (MC3T3-E1) did not show significant differences between the five analyzed samples, at any of the concentrations.
- All the obtained powders (HA1, HA_HT_12, HA_HT_48, HA_CP_12, HA_CP_48) are made up of nanometric polycrystalline particles with single phase carbonated hydroxyapatite with insignificant compositional and textural differences. The hydrothermal treatment at high temperature (200°C) and a complete cycle duration of 60 minutes, led to obtaining a carbonated apatite powder, sample HA1, with numerous anionic and cationic substitutions determined by the presence of trace elements in the crystalline structure, with polycrystalline particles having the morphology of bars with an average length of 77 nm and an average diameter of 21 nm, with high mesoporosity (intra and inter-particles), created by spherical pores with diameters <10 nm.

The HA1 powder was also comparatively characterized alongside two xenograft granular samples, Bio-Oss® originating from fully deproteinized bovine cortical bone and Gen-OS® originating from deantigenized porcine bone, widely used as bone grafting materials in dental practice.

- The HA1 powder showed a great compositional similarity compared to the two xenografts, with greater differences compared to Gen-OS®, where the remanence of the protein phase in the form of mineralized collagen fibers induces compositional differences, especially marked in the FTIR spectra, but and morpho-structural compared to the other two samples containing only the mineral phase of the bone (Figure 4).

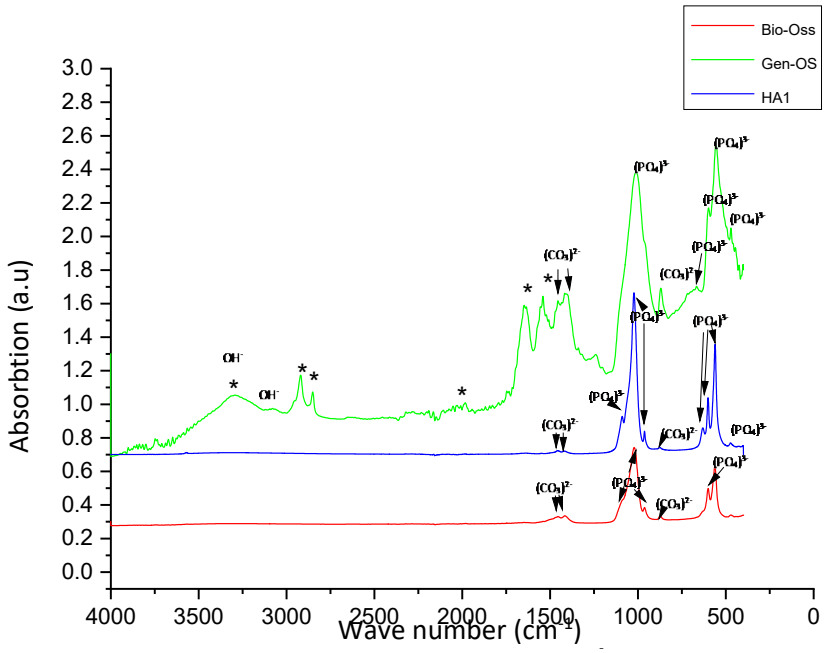

Figure 4 FTIR absorption spectra for Bio-Oss, Gen-Os and HA1 samples;(*) absorption bands for functional groups characteristic to collagenous proteins

- TEM images and SAED patterns highlighted the nanometric size and poly-crystallinity of the HA1 particles as well as the Bio-Oss® and Gen-OS® xenograft samples, the superior porosity, in the mesopores area, of the HA1 particles, induced by the treatment hydrothermal, compared to the mammalian bone samples (Figure 5). Also, the morphology of the particles is different in the three analyzed samples: while the HA1 sample contains only polycrystalline particles with the shape of nanorods (Figure 5F, G, H), the Bio-Oss sample mostly contains particles with a nanorod morphology but also polyhedral plates (Figure 5A, B, C), and in the Gen-OS sample, the hydroxyapatite particles in the shape of elongated bars can hardly be identified (Figure 5D, E), these being blurred by the presence of collagen fibers. The longest length of the bar-shaped particles was identified in sample HA1 (Table 2).

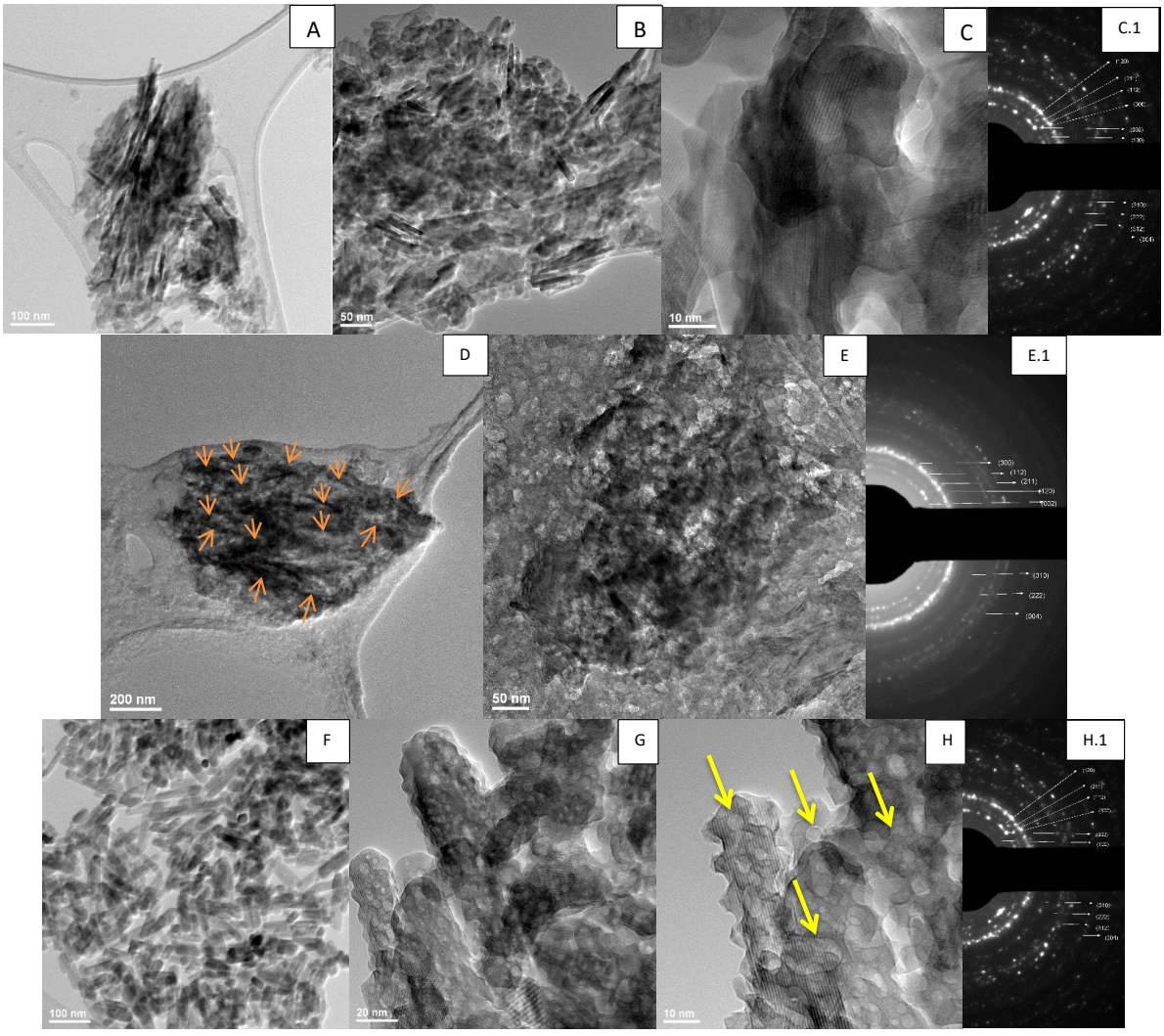

Figure 5 TEM images (A-C) Bio-Oss, (D-E) Gen-Os, SAED patterns of the Bio-Oss (C.1), Gen-Os (E.1) şi HA1 (H.1) samples.

Table 2 Hydroxyapatite particles sizes contains into Bio-Oss, Gen-Os and HA1 from TEM images

Particles sizes	Bio-Oss	Gen-Os	HA1
Minimum diameter (nm)	10.25	17.76	21.74
Maximul diameter (nm)	14.1	26.45	27.18
Minimum length (nm)	50.41	77.29	74.32
Maximul length (nm)	72.23	107.16	116.49
l/d ratio	4.9	4.4	3.4

- The cytotoxic behavior of the three comparatively analyzed materials showed that HA1 induces cell viability and oxidative stress compared to the control samples (only AFSC cell culture), lower than the Gen-OS® sample, and Bio-Oss® showed a atypical cytotoxic behavior, with the values of oxidative stress and cell viability below the values of the CTRL samples (Figure 6 A, B).

A)

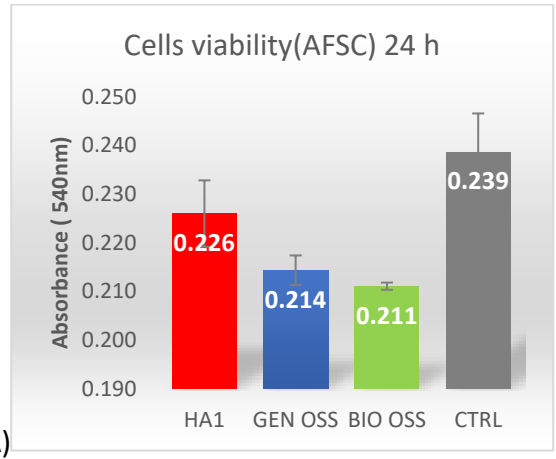

B)

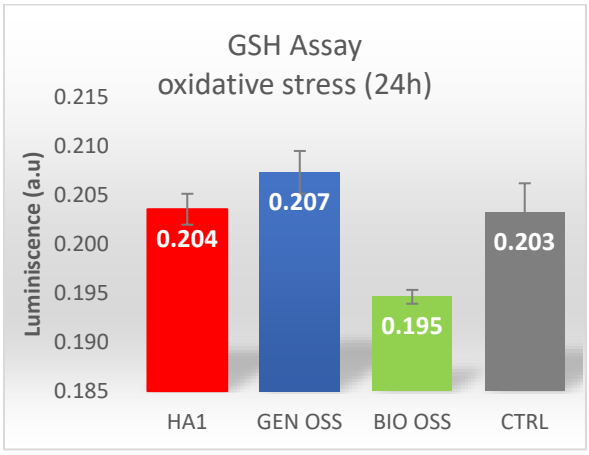

Figure 6 *A) MTT Assay: absorbance at 540 nm for AFSC culture in the presence of HA1, Gen-Os, Bio-Oss powders and CTRL sample (only cells), B) GSH Assay evidence the AFSC oxidative stress in the presence of HA1, Gen-Os, Bio-Oss and CTRL (only cells) after 24h incubation time . Results are presented as the mean of three trials ± S.D; p<0.05/n (n=6) based on ANOVA statistical data, followed by post hoc Bonferroni t- test corrections*

Following these results, it was concluded that HA1 powder is the best candidate to be used as a bone augmentation material, either in powder form or shaped in the form of porous or dense scaffolds. In addition, the addition of some biopolymers to the HA1 powder can potentiate the biocompatibility and moderate bioactivity characteristics, improved adhesion of proteins and cells to the biomaterial, which lead to an increase in the osteoconductive effect and even osteopromoting mechanisms.

CAPITOLUL 4 POTASIUM SODIUM NIOBATE ($K_xNa_{1-x}NbO_3$) POWDERS: SYNTHESIS AND COMPOSITIONAL AND MORPHOSTRUCTURAL CHARACTERISATION

In the chapter 4, was presented the synthesis method of different compositions of sodium and potassium niobate powders, using a wet hydrothermal route assisted by microwaves, with kinetics not fully elucidated, aiming to establish the process parameters to obtain compositional reproducibility and predictability. In the second part of the Chapter 4, a compositional and morpho-structural characterization of all 15 samples of solid solutions was carried out, trying to identify and confirm the molar fraction x of $K_xNa_{1-x}NbO_3$, in order to establish the precursor concentrations and the technological parameters necessary to obtain the composition of the solid solution $K_{0.5}Na_{0.5}NbO_3$.

The synthesis of sodium and potassium niobate powder with the best piezoelectric properties was pursued for use in the synthesis of biocomposites in the HA-KNN-CS system. For the synthesis of the solid solution powder of sodium and potassium niobate with a composition as close as possible to $K_{0.5}Na_{0.5}NbO_3$, at the limit of the O-T morphotropic phase, the wet phase synthesis method was used through the hydrothermal method assisted by microwaves, which allows limiting the size of the particles to nanometers and submicrons, avoiding the formation of secondary phases or unconsumed reactants by controlling the treatment duration, reduced duration and low treatment temperatures compared to the classic wet phase synthesis method, thus a reduced energy consumption. It started from a mixture of alkaline solutions of KOH + NaOH, in four series of molar ratios (K/Na= 8M/8M, 8M/4M, 7M/3M and 6M/4M) and Nb_2O_5 powder, having a low reactivity for wet synthesis routes. The variables applied in the technological process were the temperature 200-250°C (technologically limited as a maximum value), temperatures suited to the objective of maintaining the coexistence of crystalline phases O and T, at room temperature; the duration of the plateau at the maximum temperature of 30, 60, and 90 minutes allowed the identification of the necessary durations of time in the hydrothermal cycle to reach equimolarity between K and Na in $K_xNa_{1-x}NbO_3$; the high pressure of 40 bars was a constant of the hydrothermal process and aimed at catalyzing the kinetics of the formation of the solid solution on the perovskite structure. Of all the sample series, only K8N2 benefited from the comparison of the hydrothermal treatment at the two temperatures.

The compositional characterization of the synthesized powders was carried out by determining the X-ray fluorescence (XRF) spectra by estimating an average formula of the $K_xNa_{1-x}NbO_3$ solid solution for each of the 15 synthesized samples, then with the help of X-ray diffraction analysis, Raman spectroscopy, and SEM-EDS spectroscopy, an attempt was made to confirm the estimates for the values of the ratio between K and Na (molar fraction x) in the 15 perovskite networks obtained by varying the concentration of the precursors and changing the duration of the bearing and the temperature of the hydrothermal treatment.

The results of the XRF analysis revealed that the solid solution powders with the average compositions closest to $K_{0.5}Na_{0.5}NbO_3$ were generated by the samples: K8N2_250_30 ($K_{0.47}Na_{0.53}NbO_3$), K7N3_200_30

($K_{0.43}Na_{0.57}NbO_3$) and K8N8_200_90 ($K_{0.44}Na_{0.56}NbO_3$). The 15 synthesized specimens were represented in the $KNbO_3$- $NaNbO_3$ binary diagram for a better overview (Figure 7).

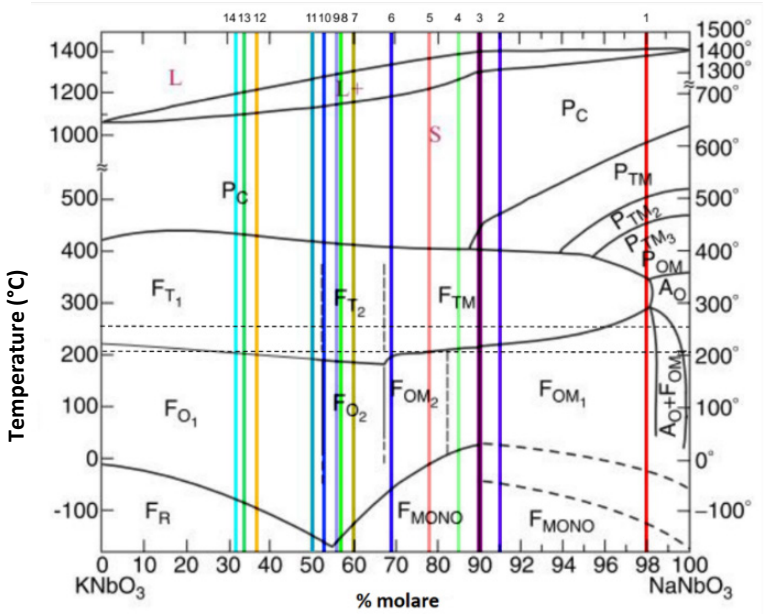

Figure 7 The 1-15 samples placement in the $KNbO_3$-$NaNbO_3$ binary diagram [26]: 1-K8N8_200_30; 2-K6N4_200_90 and K8N2_200_90; 3- K8N8_200_60; 4-K6N4_200_60; 5- K6N4_200_30; 6- K7N3_200_90 ; 7- K7N3_200_60; 8- K7N3_200_30; 9- K8N8_200_ 90; 10- K8N2_250_60; 11- $K_{0.5}Na_{0.5}NbO_3$; 12- K8N2_200_60; 13- K8N2_250_30;14- K8N2_200_30 and K8N2_250_90;

- XRF Analise allowed to determine an average value of the molar fraction *x* for each of the 15 specimens, synthesized under different conditions, gave the opportunity to appreciate the conditions suitable for obtaining solid solutions with x ~ 0.5 (Figure 8 A-D). The targeted KNN ($K_{0.5}Na_{0.5}NbO_3$), at the same KOH/NaOH ratio and temperature (200°C), could be reached by the variation of dwelling time for the series of samples K8N8 after 90 minutes of HTMW treatment (*x*=0.44), for K7N3 after 30 minutes (Figure 8 A,B). (*x*=0.43) and apparently cannot rich a higher molar fraction *x* over 0.43, for the samples in series K6N4, the highest K content was 22 molar % at 30 minutes. After the short HTMW cycle, the closer x to 0.5 (x=0.47) was obtained at 250°C (K8N2_250_30), but after data extrapolation (Figure 2B) the composition $K_{0.5}Na_{0.5}NbO_3$ would be expected at 35 minutes of treatment. The same reasoning could be considered at composition K8N2 at 200°C if the HTMW dwelling time would be 67 minutes instead 60 minutes (Figure 8 C,D).

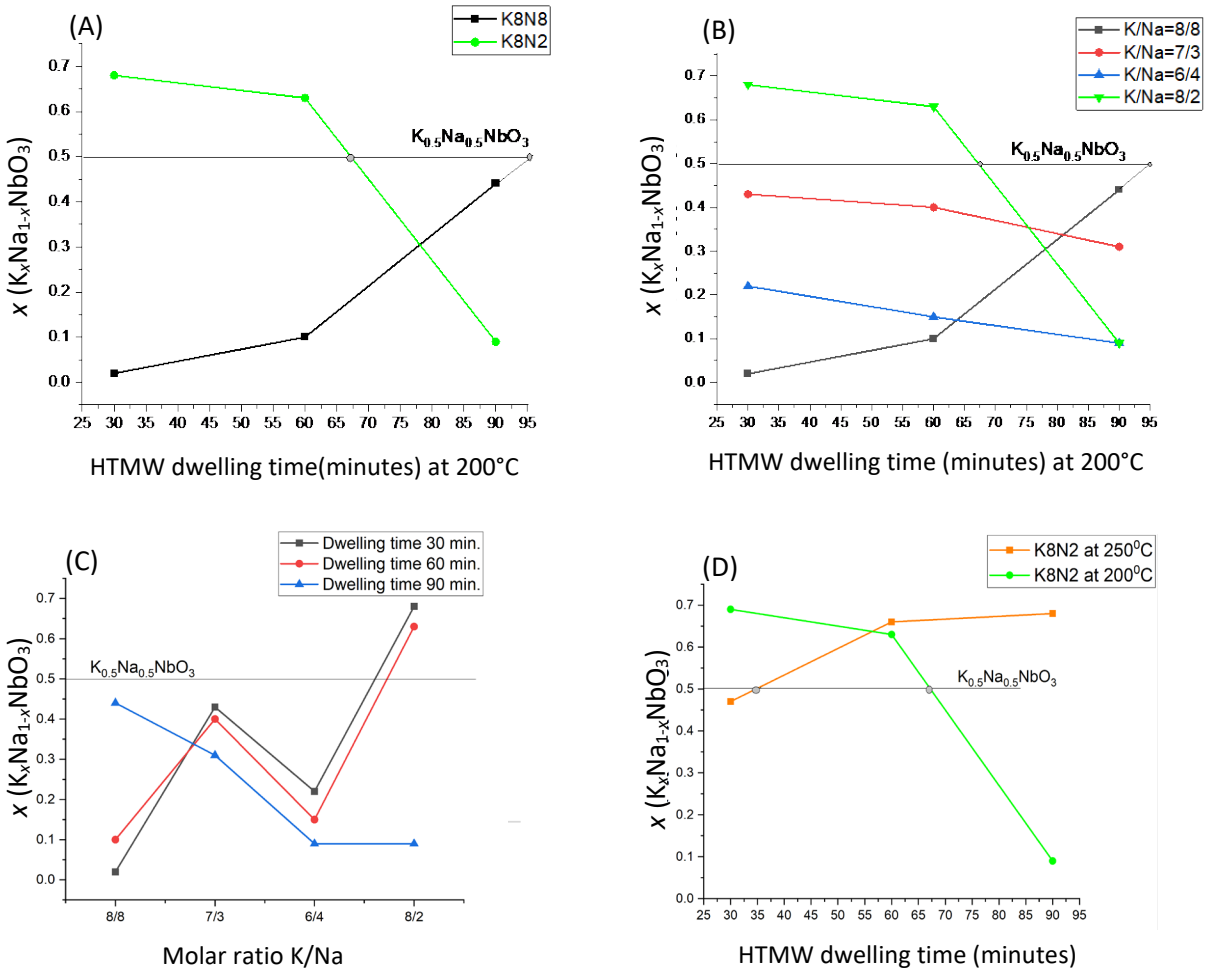

Figure 8 Solid solution $K_xNa_{1-x}NbO_3$ molar fraction *x* variation depending on HTMW dwelling time (30-90 minutes) at maximum temperature 200°C, for different alkaline precursor mix molar rate (A) K8N8 sample vs. K8N2 (KOH-8M); (B) samples K7N3, K6N4, and K8N2 (KOH+NaOH=10M), (C) Molar fraction *x*($K_xNa_{1-x}NbO_3$) variation depending on alkaline precursor mix molar rate for the three series of HTMW dwelling time (30, 60 and 90 minutes) at maximum temperature 200°C; (D) solid solution $K_xNa_{1-x}NbO_3$ molar fraction *x* variation for sample K8N2(K/Na= 8M/2M) depending on the HTMW temperature 200°C and 250°C at the three tested dwelling time (30, 60 and 90 minutes).

- X-ray diffraction analysis revealed the formation of solid solution phases, the absence of secondary phases (sodium niobate or potassium niobate, as well as unreacted niobium oxide), the coexistence of crystals in O and T symmetry, but the exact composition could not be identified synthesized solid solutions. However, it was confirmed that solid solutions with $x > 0.5$ have a perovskite structure closer to that of KNbO3, and those identified by XRF richer in Na, have diffraction peaks at 2ϑ angles close to those of the diffraction pattern of $NaNbO_3$ (Figure 9). Through Rietveld structural refinement, it was confirmed the coexistence of O and T symmetry phases in the three samples, but also the structural similarity of the crystalline networks with $K_{0.5}Na_{0.5}NbO_3$ having O and T symmetry, the crystallites of the 3 candidates do not exceed 20 nm. Repeting the syntheses for powder stock under the conditions of KOH/NaOH=8/2, 250°C, 30-minute step, demonstrated the reproducibility of the same solid solution composition

($K_{0.47}Na_{0.53}NbO_3$), the result was verified by comparing the X-ray diffractograms of independently synthesized powders, which differed only in the amplitude of the peaks positioned at the same diffraction angles.

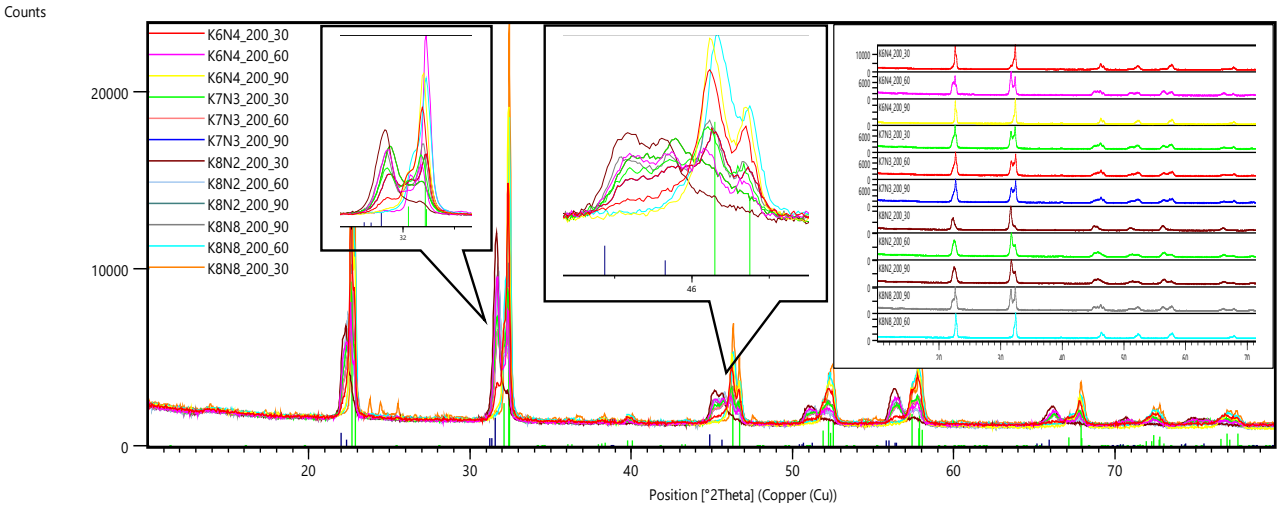

Figure 9 X-Ray Powder Diffraction plot for the samples HTMW synthetized at 200°C, 30-90 min, comparing with orthorhombic $NaNbO_3$ XRPD pattern (green, PDF 04-012-8146) and orthorhombic $KNbO_3$ XRPD pattern (black, PDF 04-014-4292), graphics displayed successively and overlapped plots with upper insert detailed sector 2ϑ= 31-33° and 44-46°, respectively.

- From the Raman spectra it was possible to confirm some findings resulted in the XRF analysis, XRD and Rietveld structural refinements, without being able to accurately determine the compositions of the solid solutions, in the absence of their paternal spectra. The interferences that appeared were created by comparing the spectra of the analyzed samples with the Raman spectra from the literature of sodium niobates, potassium niobates synthesized by classical methods having a single O or T phase. However, it was possible to determine the vibrations characteristic of Na-O bonds from wave numbers 68 - 73 cm^{-1} and K-O at wave numbers <60 cm^{-1}, more intense as the content of K or Na increased in $K_xNa_{1-x}NbO_3$. The peak of the Nb-O bond tightening vibrational mode, A1g (v1) from 610-612cm^{-1}, is sensitively influenced by the modification of the O-Nb-O angle within the NbO6 octahedra and the shortening of the Nb-O distance, which occurs when the lattice symmetry changes from orthorhombic to tetragonal. These transformations are marked by the splitting or appearance of a shoulder of the high intensity peak from ~ 600 cm^{-1}, due to the intensification of the Eg (υ2) tightening vibrational mode at 569-572 cm-1[27]. In the tetragonal phase the broad peak is splits and becomes sharper at the transition to a form of reduced symmetry (O)[28]. A higher FWHM value is related to a high crystallinity but also to a higher content of the low symmetry orthorhombic phase [28, 29]. This behavior seems to be caused by the decrease in the internal stress determined by the lengthening of the distance between the Nb5+ ions and the coordinated oxygen ions, the rotation of the octahedra and the increase in the parameters of the orthorhombic network compared to

the tetragonal one (a, b and c)[27]. It is known that, in the orthorhombic and tetragonal polymorphic phases, a different inclination of the NbO_6 octahedra was reported, which was also observed in the XRD results where, after Rietveld structural refinement, the orthorhombic phases had a larger unit cell than the tetragonal one[27].

- The SEM micrographs revealed well-crystallized agglomerations with cuboidal morphology formed by coalescence, with maximum dimensions of up to 2.9 µm in weight of up to 1% and average sizes between 98 - 464 nm, with the majority weight between 100- 300 nm. A dependence was found between the average size of the particles and x in the sense that solid solutions with an average K content greater than 0.5 but also those containing a greater weight of the O phase have average sizes closer to the 300nm limit. It was also found that the higher temperature of the hydrothermal treatment of 250°C can potentiate the increase in the average size of the granules, for example the sample K8N2_200_30 has an average size of the granules of 116±12.23nm and K8N2_250_30 of 301±30.29nm, but it is not verified at K8N2_200_60 (181±10.7 nm) *vs.* K8N2_250_60 with 221±11.2 nm or K8N2_200_90 (464±11.6 nm) and K8N2_250_90 (369±19.6 nm). Moreover, even the increase in the duration of the hydrothermal treatment from 30 to 90 minutes does not determine the formation of larger crystals, for example in the K7N3 series at 200°C for 30 minutes the average size is 275 nm at 60 minutes it is 98.5 nm and at 90 minutes 403 nm, due to the dissolution processes that occur in the reaction medium during the microwave-assisted hydrothermal treatment that leads to the modification of the K and Na content of the solid solutions. Thus, the finding was that the duration and temperature of the treatment associated with the effect of microwave energy will influence the evolution of the mole fraction *x* of $K_xNa_{1-x}NbO_3$, which will dictate the greater or lesser weight of the O or T crystalline phase, the size of the crystallites developed in the O network being larger than the T ones, thus leading to larger dimensions of the cuboid shaped particles (Figure 10). The average particle size of $K_xNa_{1-x}NbO_3$ was determined by measurements from SEM images, and those of the crystallites were obtained following Rietveld structural refinement.

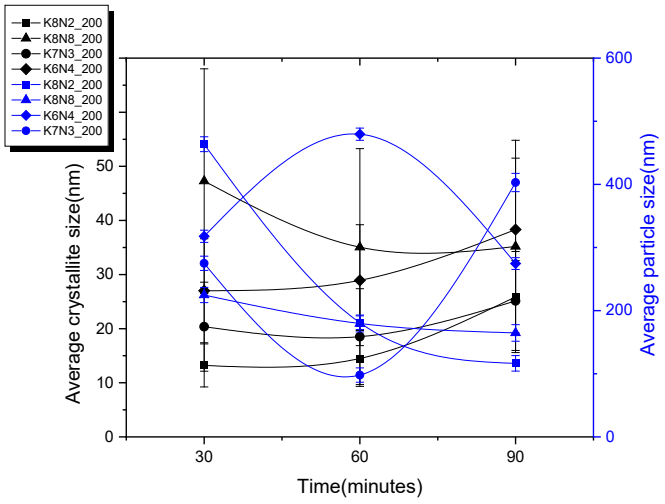

Figure 10 Average crystallite and particle size of all series of samples at 200°C depending on the HTMW dwelling time (30-90 min.).

- The piezoelectric coefficient of each solid solutions composition was determined in non-conventional conditions, on green, non-polarized KNN powder discs. A selection of 5 samples having the same dwelling time (30 minutes) and temperature 200 and 250°C (S1 K8N2_250_30, S2 K8N2_200_30, S3 K7N3_200_30 , S4 K6N4_200_30, S5 K8N8_200_30) was carried out in order to observe d_{33} variation for representative samples(Figure 11 A-C) . As expected, the highest value of d_{33} was recorded for K8N2_250_30 having the estimated formula $K_{0.47}Na_{0.53}NbO_3$, followed by K7N3_200_30 with $K_{0.43}Na_{0.57}NbO_3$. The closest compositions to $K_{0.5}Na_{0.5}NbO_3$ and the highest values of d_{33} of 0.8 pC/N at the frequency of 110 Hz was observed for sample K8N2_250_30 that generates a solid solution with x =0.47, with O and T crystals symmetry coexistence. The lowest d_{33} value was recorded for sample K6N4_200_30, at all frequencies tested. The voids, pores, cracks in the structure of ceramic bodies concentrate the electric charge, preventing the movement and concentration of the mobile charge towards the surfaces of the material, generating a weak piezoelectric response to the mechanical load, thus a low value of d_{33}. The relative density measured on the raw cylindrical bodies does not exceed 65%, consequently the surfaces of the samples do not concentrate the load density generated by the compression applied to them, and the value of the coefficient is well below the d_{33} values reported for sintered and polarized KNN [30, 31]. Also, the polarization of the material aims to increase the charge density on the free surfaces of the cylindrical samples, through external electrical stimulation, with positive results on the values of the piezoelectric effect. The measurement of the piezoelectric constant on raw samples, under non-conventional conditions, had the purpose of assessing whether the composition of the solid solution influences the d_{33} value, even for powders insufficiently densified.

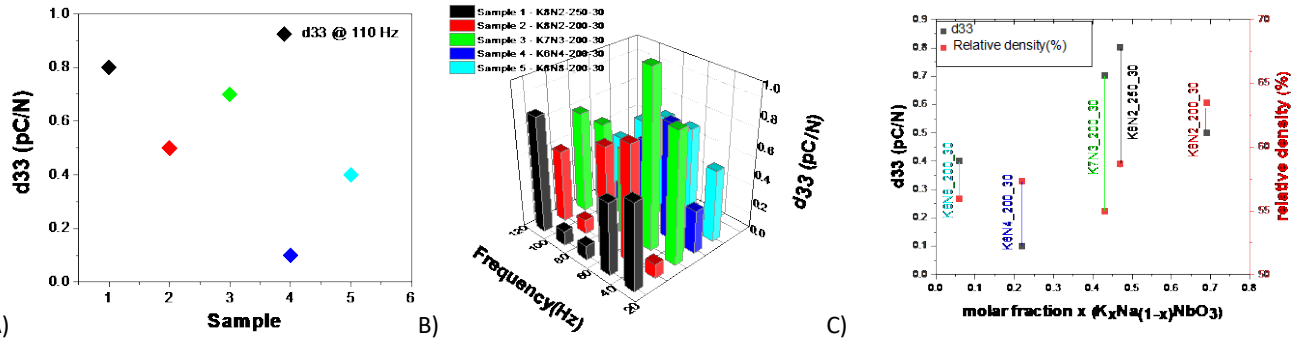

Figure 11 Piezoelectric constant d_{33}(A) for K8N2_250_30 (Sample 1), K8N2_200_30 (Sample 2) , K7N3_200_30 (Sample 3), K6N4_200_30 (Sample 4), K8N2_200_30 (Sample 5) at 110Hz, (B) d_{33} variation with frequency (30-110 Hz) (C) d_{33} variation with molar fraction x and the relative density of unsintered discs

CAPITOLUL 5 HA-KNN-CSL1.5 COMPOSITE POWDERS, HYDRO-GEL, AND SCAFFOLDS: SYNTHESIS AND COMPOSITIONAL AND MORPHOSTRUCTURAL CHARACTERISATION

The synthesis of composites in the HA-KNN-CS system involved obtaining chitosan hydrogels from the water-insoluble polymer powder, in the high molecular weight (CSH) and low molecular mass (CSL) version, by solubilization in the aqueous solution of acetic acid with a concentration of 1.5 and 3%, resulting in three chitosan hydrogels CSL_3, $CSL_{1.5}$ and $CSH_{1.5}$. This was followed by the embedding of HA and KNN powder mixtures by magnetic homogenization maintaining the ratios of 30% CS and 70% (HA+KNN) and in the case of powder mixtures varying the HA/KNN proportion to 10/90, 50/50, 90/10, leading to obtaining composites in gel form. Lyophilization of composite hydrogels was used to obtain the porous scaffold variants (Figure 12) by maintaining the composite gels for 96 h in a depression regime of p~ 0.01 mbar (vacuum) and a temperature of -70°C, the composite granules (flakes) being able be obtained from scaffolds by cryo-granulation with liquid N2 (Figure 13).

A) 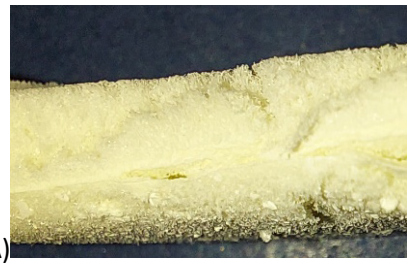 B)  C) 

Figure 12 Cross section images of 10HA-90KNN-$CSL_{1.5}$(A), 50HA-50KNN-CSL_3(B), 90HA-10KNN-$CSH_{1.5}$(C) scaffolds, after lyophilization

Figure 13 Image with flakes of 10HA-90KNN-$CSL_{1.5}$ synthetized by scaffolds cryo-grinding

- The three variants of chitosan hydrogels with the same concentration of 2% (m/v) CSL3, $CSL_{1.5}$ and $CSH_{1.5}$ were characterized. Since their preparation, it was found that the CSL_3 hydrogel has a very low viscosity (156mPa/s, 100 rpm and 24.5°C) and a too low pH (3.82), which would have created the suspicion of the segregation of the powders and could have determined decomposition of hydroxyapatite after embedding; the $CSH_{1.5}$ hydrogel, chosen for its potential to generate the best antibacterial, anti-inflammatory and hemostatic effects, created difficulties in solubilization in the 1.5% acetic acid aqueous solution even after 96 hours of homogenization, with significant amounts of insolubilized crystalline phase remaining detected in the X-ray diffractogram performed on the freeze-dried scaffolds; the $CSL_{1.5}$ gel showed the best results of stability to water absorption and disintegration, pH of 5.25, homogeneity to the inclusion of powders but also the best results of biocompatibility by the MTT test and antibacterial effect inoculated on both gram-positive bacterial cultures (*S. aureus*) and gram negative (E. coli) but also on fungal strains (*C. albicans*).
- X-ray diffraction analysis confirms the fact that between the three components of the composites, nanometric particles of HA, chitosan hydrogel with 1.5% acetic acid and KNN, no chemical reactions occur, but electrostatic interactions of the functional groups of chitosan are possible (hydroxyl, carboxyl, amino) with cations or anionic groups from HA and KNN powders. The profiles of the diffraction peaks of the composite materials are very similar to the patterns of the crystalline powders of HA and KNN, they are reduced in amplitude and much wider compared to the patterns of the embedded powders, the polymer matrix of chitosan, as an amorphous phase, blurs the diffraction of incident X-rays from the material (Figure 14).
- The diffractograms of the composites are similar as position of diffraction angles 2ϑ, the intensities of peaks raise with powders content increase in the composite. Comparing the three variants of composite matrix (chitosan) $CSH_{1.5}$, CSL_3, and $CSL_{1.5}$, the influence of the type of amorphous phase in the profile of the diffraction peaks is insignificant.

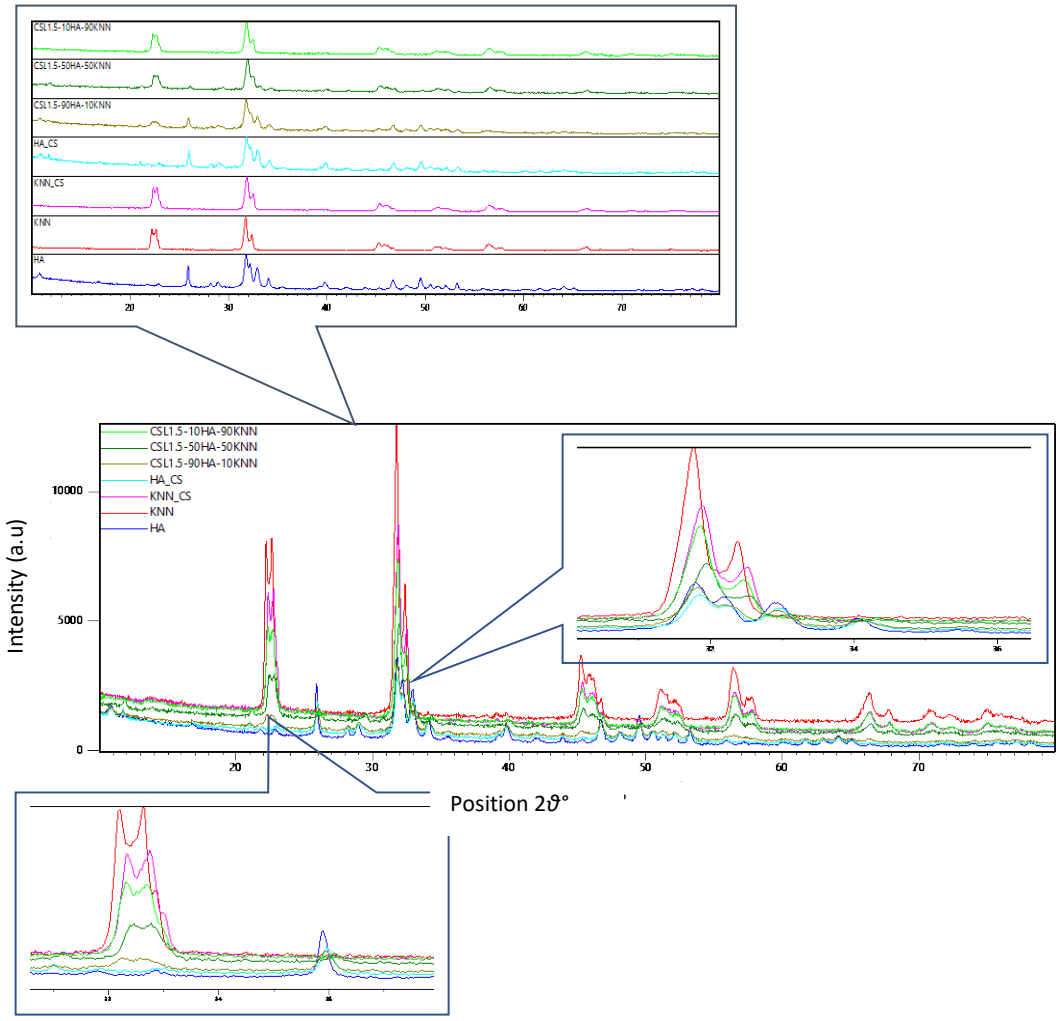

Figure 14 X- Ray diffraction patterns of lyophilized scaffolds of HA- $CSL_{1.5}$, KNN- $CSL_{1.5}$, 10HA-90KNN- $CSL_{1.5}$, 50HA-50KNN- $CSL_{1.5}$ and 90HA-10KNN- $CSL_{1.5}$

- The FTIR spectra highlighted the bonds characteristic of chitosan, the vibrations characteristic of the PO_4^{3-} groups in HA, and Nb-O-Nb in the NbO_6 octahedra of the KNN solid solution, superimposed with those of the glycosidic bond and those of the pyranose nuclei, without changing their positions. That indicate the maintenance of the three components of the composites without chemical interactions. The FTIR spectra allowed the estimation of the degree of chitosan acetylation after solubilization in acetic acid. Increasing the degree of acetylation can decrease the antibacterial effect of composite scaffolds by decreasing the positive potential of free amino groups but does not affect their hemostatic effect. However, the acetic acid present has cytostatic and anti-inflammatory action, but by increasing the solubilization of scaffolds in biological fluids, it can positively favor the rate of biodegradation of chitosan to amino acids[32, 33].

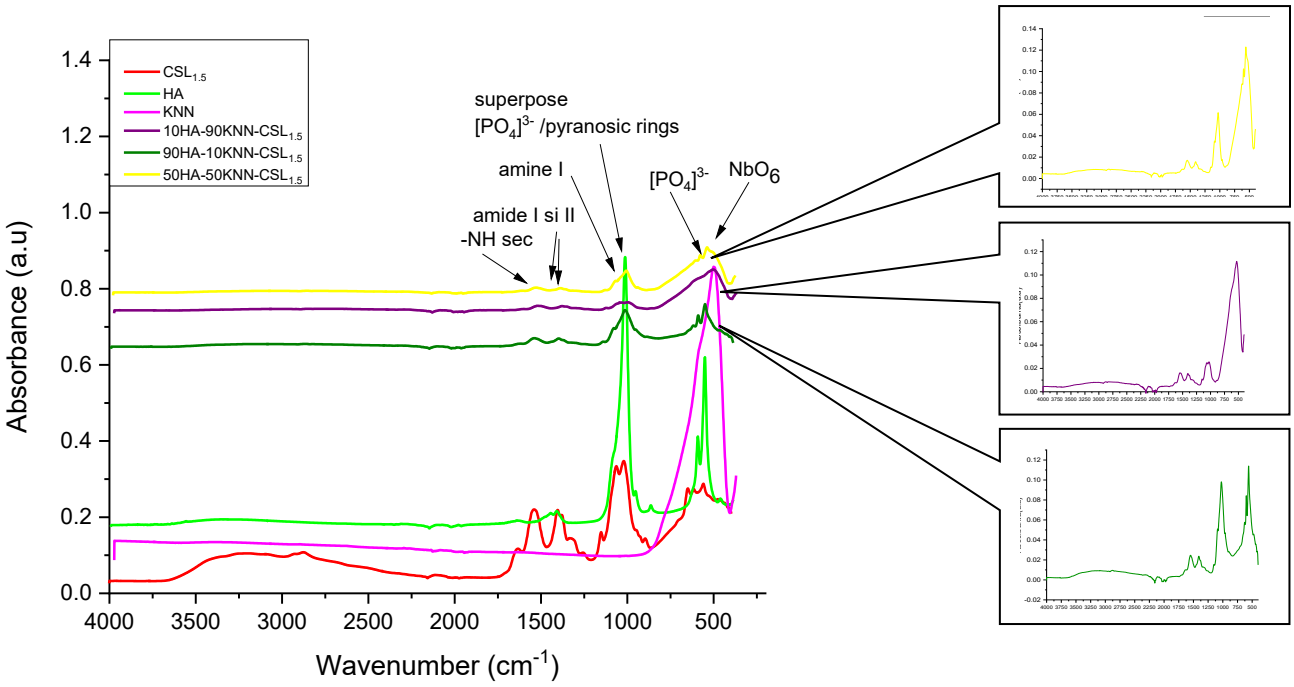

Figura 1 FTIR Spectra for composite 10HA-90KNN- $CSL_{1.5}$, 50HA-50KNN- $CSL_{1.5}$ and 90HA-10KNN- $CSL_{1.5}$ comparing with constitutive phases HA, KNN, CS

- From the BET analysis - the composites with a higher HA content have the highest specific surface because the embedded powder is mesoporous, the pores created in the freeze-dried scaffolds are mainly in the field of micropores, according to the isotherms, but the data place the maximum pore diameter at mesopores, uniformly distributed values in the distribution data show very small differences between samples. The analysis being done on the composite granules, explains the pore size findings in the macropore domain for the scaffolds. It is observed that the average level of specific surface areas of tens of square meters per gram, leads to conclusion that the pores are not interconnected and open. These findings are in agreement with the observations formulated by the scanning electron microscopy analysis regarding the porous texture of the scaffolds but also of the granules, the size of the macropores in both variants, the maintenance of the morphology of the incorporated HA and KNN powders, which can attest to the absence of chemical interactions with the formation of other unwanted phases (Table 3).

Table 3 BET and Langmuir specific surface variation and pores sizes in HA-KNN- $CSL_{1.5}$ system

SAMPLE	HA- $CSL_{1.5}$	KNN- $CSL_{1.5}$	10HA-90KNN- $CSL_{1.5}$	50HA-50KNN- $CSL_{1.5}$	90HA-10KNN- $CSL_{1.5}$
BET Specific surface(m^2/g)	13.1603 ±0.6217	8.4628 ±0.3628	18.3722 ±0.7329	21.8068 ±0.4316	24.0306 ±1.8824
Langmuir Specific surface (m^2/g)	22.0560 ±2.4558	13.9256 ±1.4344	29.5808 ±2.8841	33.2305 ±2.1907	48.8549 ±9.1257
average pore thickness- adsorption (4V/A BET)(nm)	5.0686	5.0770	5.1412	5.3601	5.1631
Average pore diameter- adsorption (4V/A) (nm)	4.5018	4.2955	4.5169	4.4808	4.9349
Average pore diameter - desorption (4V/A) (nm)	4.4955	4.4680	4.3080	4.2678	4.0609
Maximul pores diameters (nm)	154.6	158	161.2	74.6	154.6
Minimum pores diameters (nm)	1.8	1.6	1.8	1.6	1.7

- After composite scaffolds immersing in water, it was found that their macroporous structures can absorb an amount of water 20 times greater than their dry mass, and chitosan scaffolds up to 50 times greater. Insignificant differences in water absorption values appear between samples belonging to the same series (10HA-90KNN-$CSL_{1.5}$, 90HA-10KNN-$CSL_{1.5}$, 50HA-50KNN-$CSL_{1.5}$) and comparing with samples from the HA-KNN-series $CSH_{1.5}$. However, the lyophilized scaffolds of composites with the $CSL_{1.5}$ chitosan matrix, showed a better fragmentation stability when swelling following the absorption of SBF, after the first 60 minutes, which is desirable, showing in practice, a better maneuverability (Figure 15).

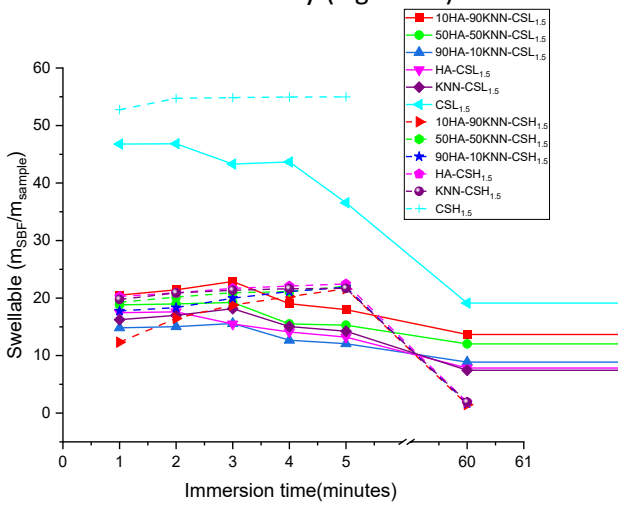

Figure 15 Swellable capacity of scaffolds composite HA- $CSL_{1.5}$, KNN- $CSL_{1.5}$, 10HA-90KNN- $CSL_{1.5}$, 50HA-50KNN- $CSL_{1.5}$ and 90HA-10KNN- $CSL_{1.5}$ in SBF

- Biodegradability of the composite scaffolds have been performed by immersing them in SBF and keeping in the incubator at 37°C for 7 and 28 days but was not determined by the mass loss method suggested in the literature [34, 35], since the scaffolds incubated for 7 and 28 days in SBF, had no longer consistency to be weighed. The incubated scaffolds were air-dried at room temperature for 48 h, in order to evaluate the biodegradation, by performing EDS elemental analyses, FTIR spectra and SEM images that could highlight new morphologies of crystalline or amorphous phases appearing as a result of possible reactions chemical decomposition or recrystallization during incubation. In all the FTIR spectra, including for the chitosan scaffolds $CSH_{1.5}$, CSL_3, and $CSL_{1.5}$ (Figure 16), the stretching vibrations for the bonds characteristic of aceto-glucosamines, where the degradation of the polymer chains is manifested, even in the absence of enzymes, possibly by acid hydrolysis. The absorption bands located between 500-1100 cm^{-1} represent the vibrations characteristic of the functional groups PO_4^{3-} or of the NbO_6 octahedra in the HA and KNN powders, which overlap the vibrations of the glycosidic bonds or the C atoms in the saccharide cores. Compared with the FTIR spectrum of the composite samples before incubation in SBF (Figure 17).

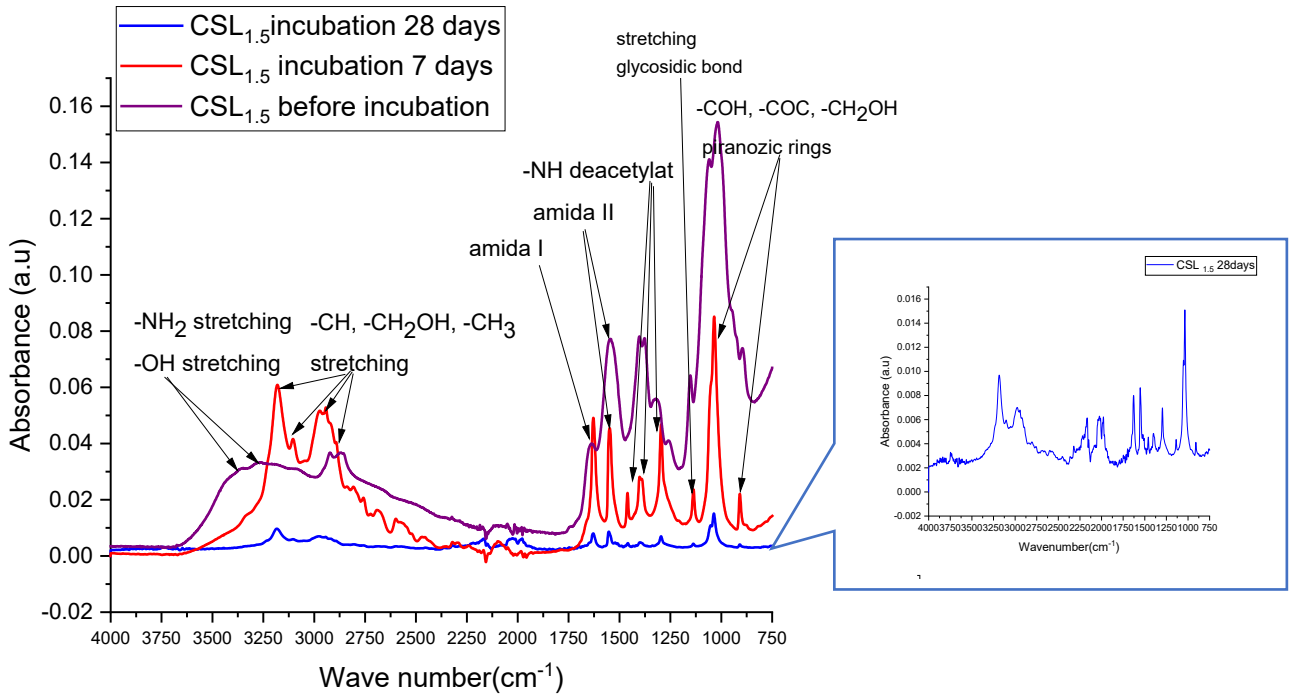

Figure 16 FTIR spectra for $CSL_{1.5}$ scaffolds before and after 7- and 28-days immersion in SBF

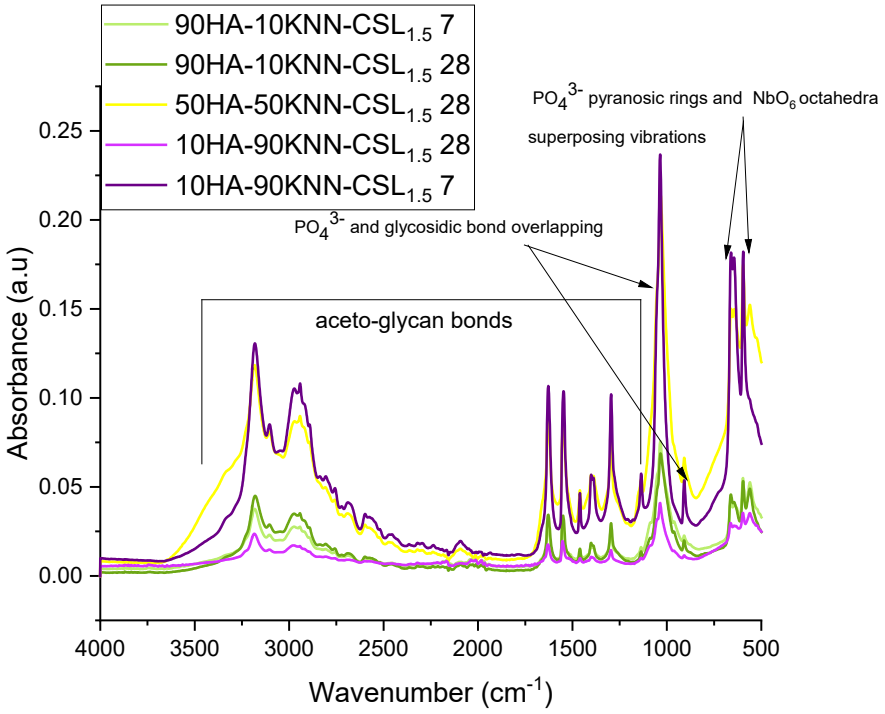

Figure 17 FTIR Spectra for composite scaffolds 90HA-10KNN-CSL$_{1.5}$, 50HA-50KNN-CSL$_{1.5}$ and 10HA-90KNN-CSL$_{1.5}$ after 7 and 28 days immersion in SBF

- The SEM images highlight the change in the surface morphology of the scaffolds after incubation in SBF:
  - after 7 days, marking the degradation of the polymer and the surface exposure of HA and KNN particles, also highlighted by the high percentages of Ca, P, Nb, K on the scanned surfaces (Figure 18);
  - after 28 days, chitosan is advanced degraded by changing the texture of the surface of the scaffolds which marks the crystallization of adsorbed salts and by decreasing the content of organic compounds containing elements such as C and O (Figure 19).

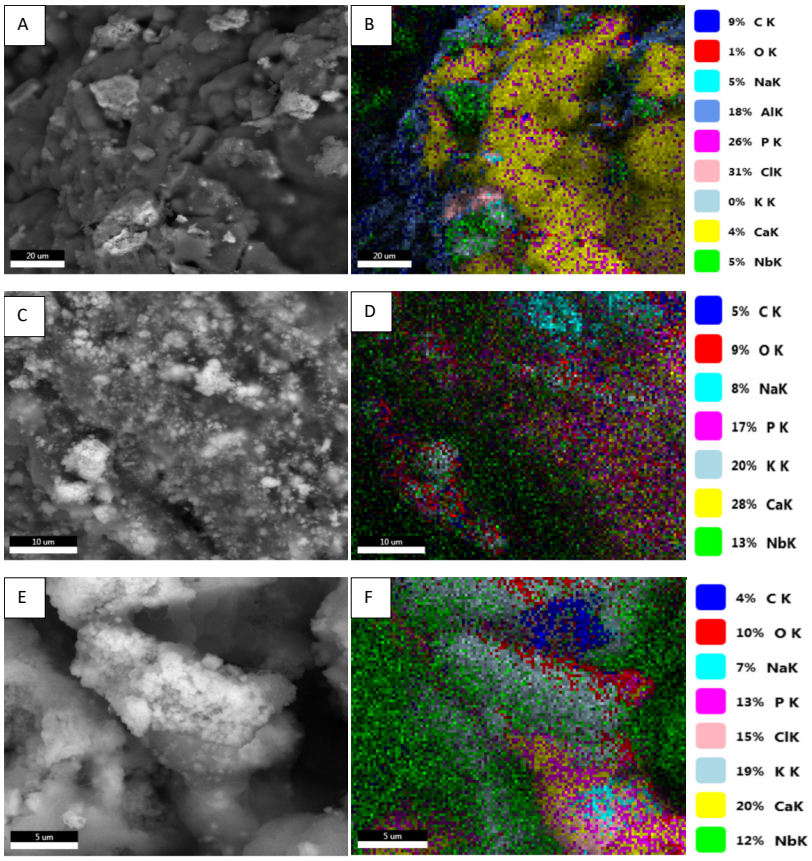

Figure 18 SEM Images (1000x, 2000x, 5000x), mapping for EDS elements distribution on the surface of the HA-KNN-CSL$_{1.5}$ scaffolds immersed in SBF for 7 days (A,B) 10HA-90KNN-CSL$_{1.5}$ (C,D) 50HA-50KNN-CSL$_{1.5}$ (E,F) 90HA-10KNN-CSL$_{1.5}$

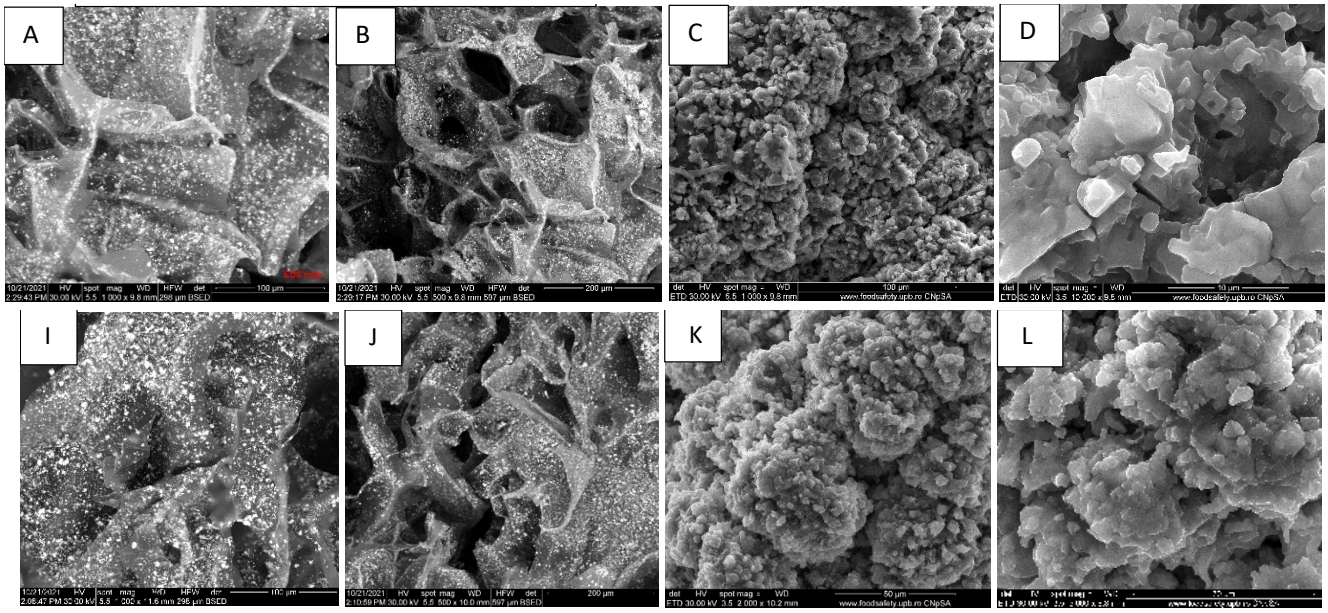

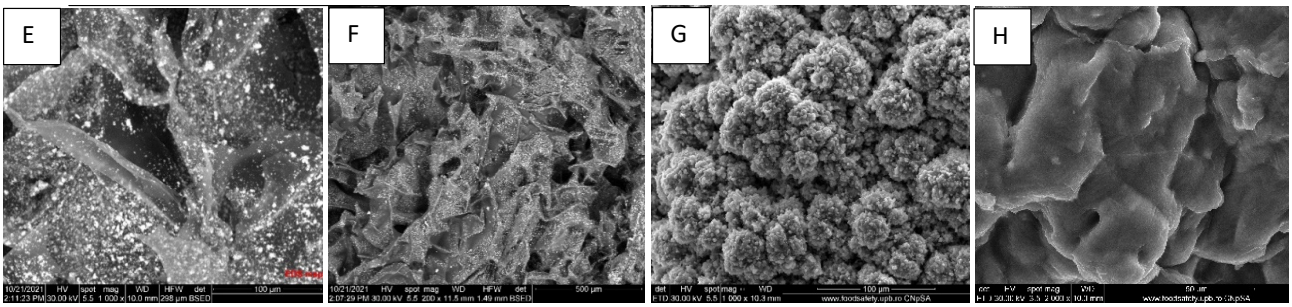

Figure 19 SEM Images and EDS elemental analysis for HA-KNN-$CSL_{1.5}$ composite scaffolds before and after 28 days incubation in SBF

The SEM images show the densification of the scaffolds and the intact preservation of the morphology of the KNN and HA granules, even if losses of the cation content (Ca respectively Na and K) from the crystalline lattice of the embedded powders, are expected.

- In chitosan gels ($CSH_{1.5}$, CSH_3, $CSL_{1.5}$, CSL_5) the antibacterial and antifungal effect increases with the acetic acid concentration increasing. The quantity of chitosan contained is the same in all samples. The concentration of acetic acid in chitosan hydrogels dictate their pH values, and together with gels viscosity those induce its diffusion footprint and the microbial culture interaction area. For this reason, samples containing high molecular mass chitosan did not exert better antimicrobial effects than low molecular mass chitosan, which reportedly contains fewer amino (cationic) groups than the former (Figure 20).

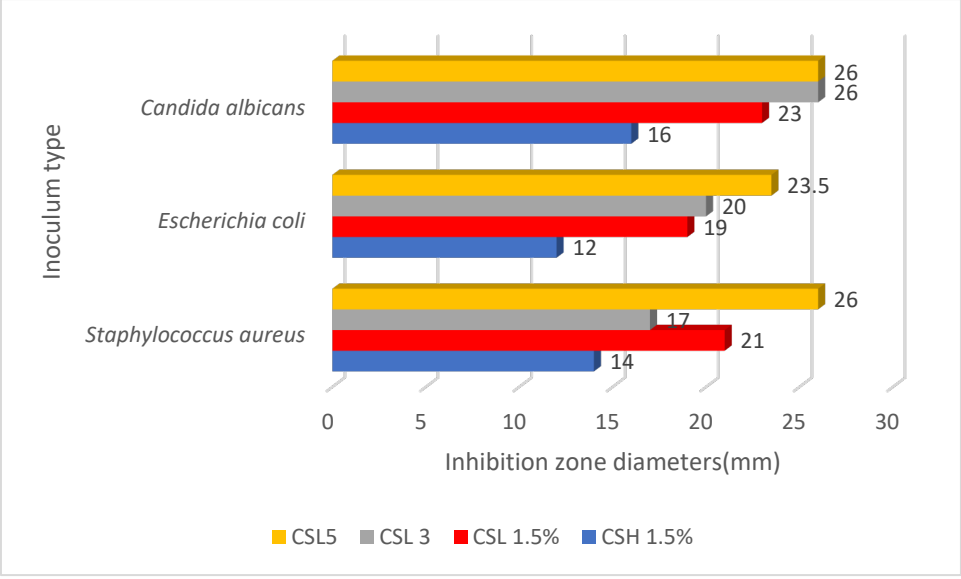

Figure 20 The inhibition zone diameter measurement using the diffusion method for antibacterial effect against *S. aureus, E. coli* and *C. albicans*, by through spot inoculation for CSL and CSH hydrogels samples solubilized in 1.5, 3 and 5% acetic acid

The obtained results showed that the sample $CSL_{1.5}$ exerted the best antimicrobial activity against all 3 strains (*S. aureus, E. coli, C. albicans*), having the inhibition zone diameter of 21 mm, 19 mm and 23.5 mm respectively (Figure 20).

Composite gels exhibit a greater antibacterial activity with the increasing content of piezoelectric powder, even in the absence of external stimulation (Figura 23).

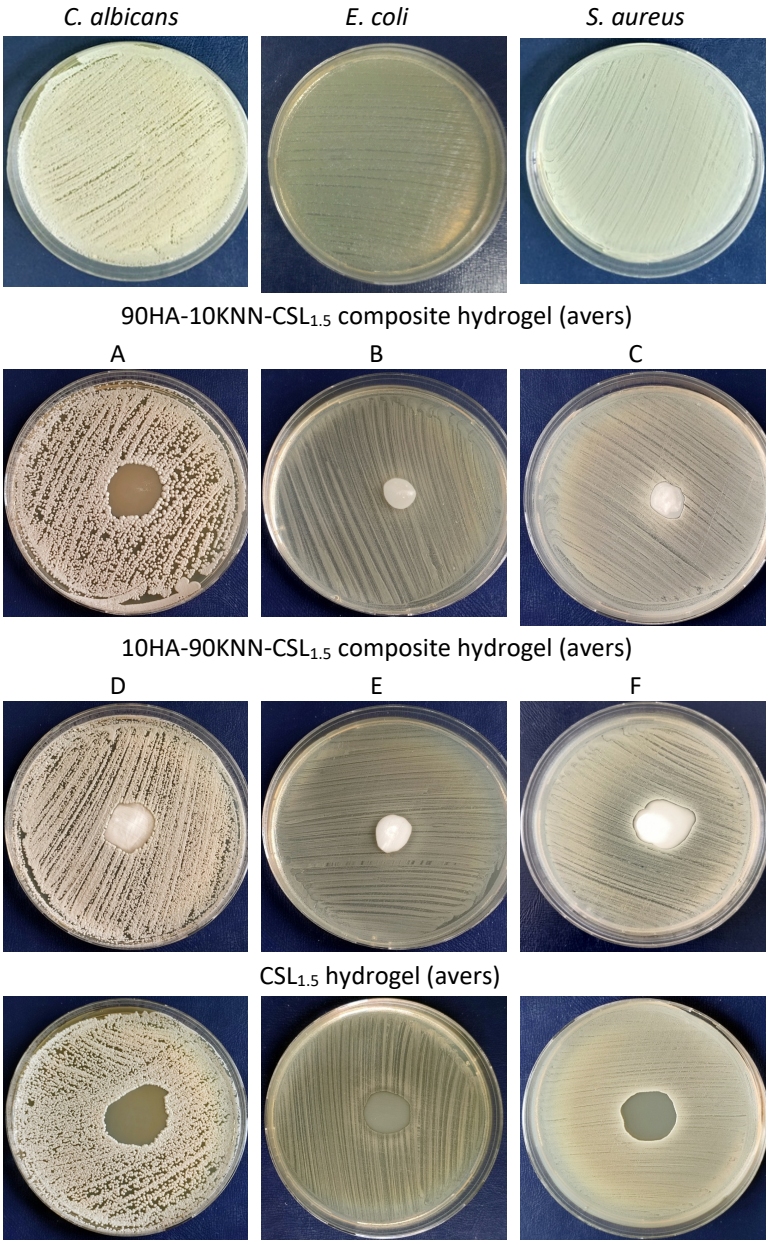

Figure 21 Images with the antibacterial effect against *S. aureus, E. coli* and *C. albicans*, by inhibition zone diameter measurement using the diffusion method through spot inoculation for 10HA-90KNN-CSL$_{1.5}$ and 90HA-10KNN-CSL$_{1.5}$ hydrogels samples

The antibacterial action of the piezoelectric KNN powders embedded in the polymer matrix can be amplified under the conditions of utilizing the piezoelectric effect, upon the application of a mechanical stress that leads to the surface polarization of the solid solution granules. Although this external stimulus was not applied to the tested samples, the 10HA-90KNN-$CSL_{1.5}$ gel shows an inhibition zone larger of gram-positive bacteria (*S. aureus*), even larger than the $CSL_{1.5}$ gel, and a more weak antibacterial effect on *E.coli*. The two composite gels showed antifungal effects similar to $CSL_{1.5}$ gel. [23, 36, 37](Figure 22).

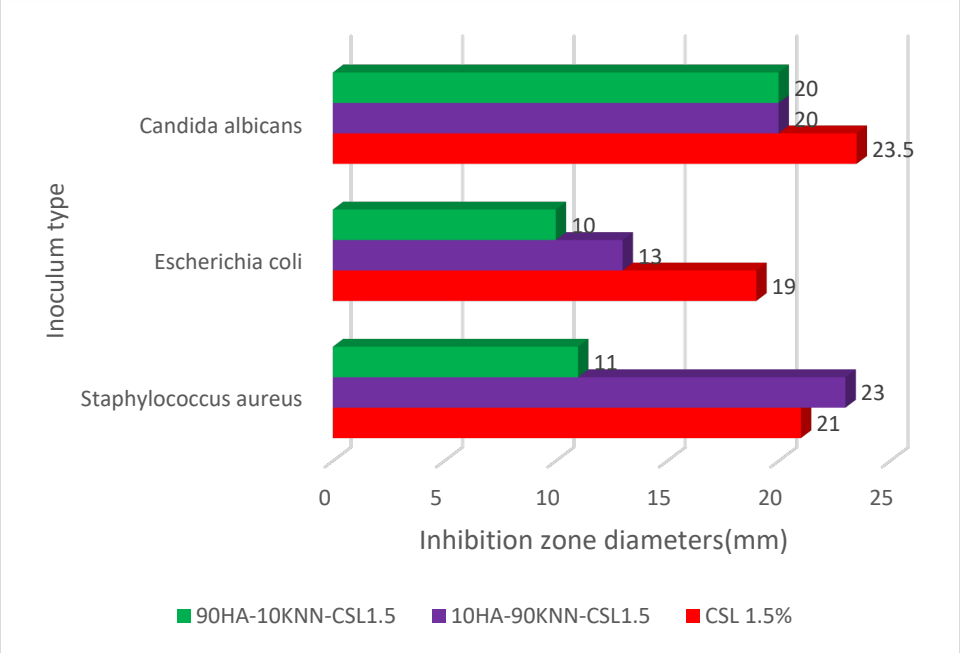

Figure 22 The inhibition zone diameter measurement using the diffusion method for antibacterial effect against *S. aureus, E. coli* and *C. albicans*, by through spot inoculation for 10HA-90KNN-$CSL_{1.5}$ and 90HA-10KNN-$CSL_{1.5}$ composite hydrogels samples comparing with $CSL_{1.5}$ chitosan gel

Composite scaffolds show very weak antibacterial activity, even those with the highest KNN content. Dry scaffolds placed in direct contact with the bacterial culture medium, according to the test protocol, create a moisture deficit that will not inhibit chemical interaction and diffusion of polarized molecules [38, 39].

- Cell viability in the presence of individual HA and KNN powders was superior to the CTRL sample (13% over CTRL) the powders inducing a moderate increase in the activity of MG-63 osteoblast cells (Figure 23). However, the biocompatibility of KNN powders with MG-63 cells was slightly lower than that of HA powder, which was expected. The biocompatibility of the HA and KNN powders was reflected in the results of the MTT test at 24h for the composite samples in the form of scaffolds and gels.

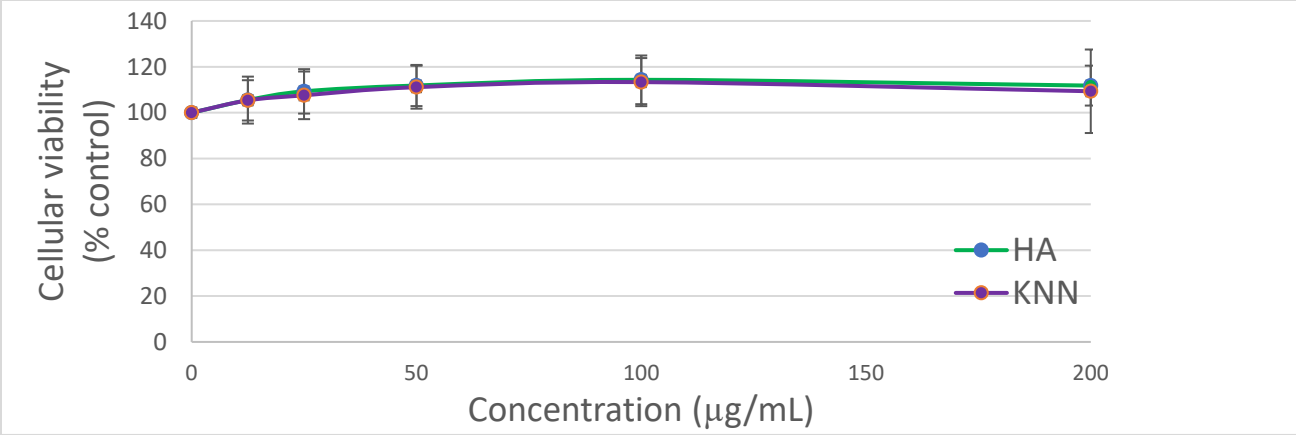

Figure 23 The MG-63 osteoblast like viability in contact with different HA and KNN powders concentrations (0-200 µg/mL) by MTT Assay after 24 h.

Thus, it can be appreciated that the scaffolds (Figure 24) or biocomposite gels did not have a cytotoxic behavior against MG-63 cell cultures, on the contrary, they exerted an effect on the cells to improve their activity, during the short incubation period (24h) .

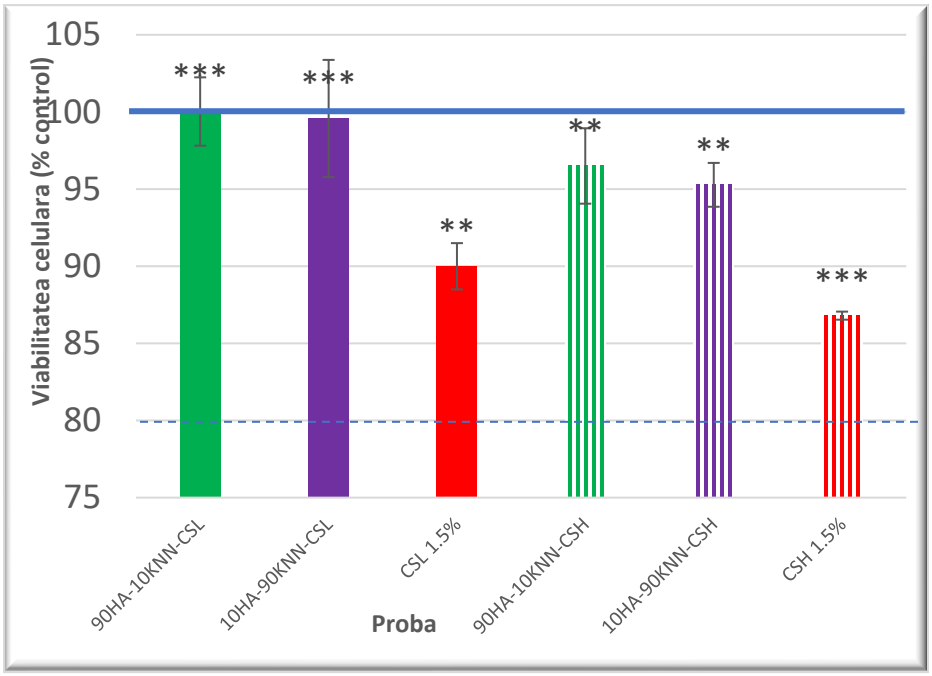

Figure 24 The MG-63 osteoblast like viability by MTT Assay after 24 h incubation in the presence of composite scaffolds series HA-KNN-$CSL_{1.5}$ comparing with series HA-KNN-$CSH_{1.5}$ composite scaffolds

Very high values of cell viability showed the composites in the form of gels compared to the scaffolds with similar compositions (Figure 25). The dry scaffolds put in contact with the cell culture medium,

according to the protocol, absorbed a quantity of water creating a deficit in the humidity of the medium cell culture, disrupting their activity in the area adjacent to the scaffolds.

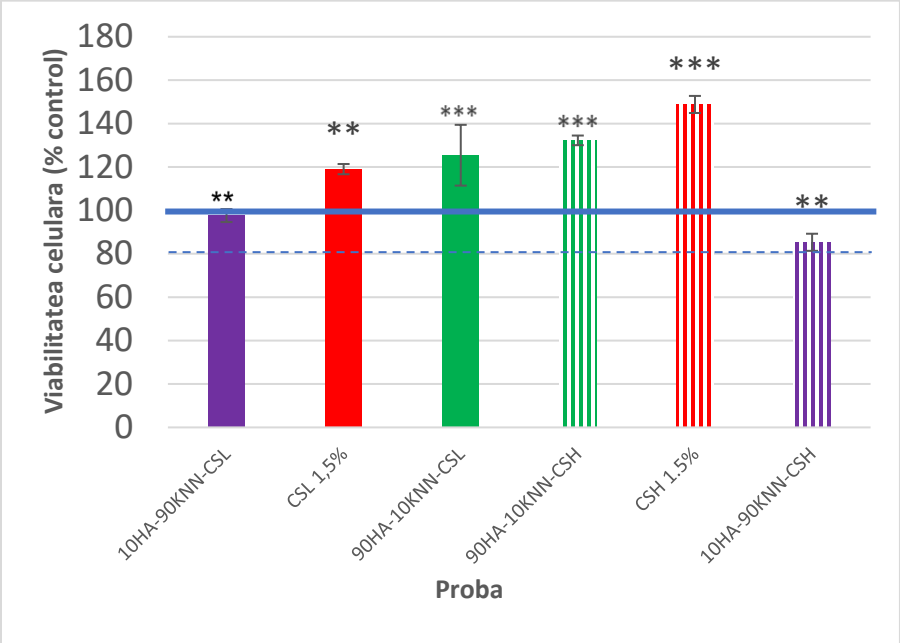

Figure 25 The MG-63 osteoblast like viability by MTT Assay after 24 h incubation in the presence of composite gels series HA-KNN-$CSL_{1.5}$ comparing with series HA-KNN-$CSH_{1.5}$ composite gels

Appreciated by the MTT test, a too high cell viability can be the result of an oxidative stress created by the incubated biomaterials even after a short time. Thus, viability translates into a much more intense metabolic activity of cells to synthesizes reductaze enzyme for the annihilation of free radicals or reactive oxygen species (ROS). The gels of all analyzed compositions contain a concentration of 1.5% acetic acid, which in scaffolds is removed by lyophilization. It has a demonstrated anti-tumor action. The higher reactivity of the gels towards the scaffolds is determined on the one hand by the higher water content that increases the interaction between the sample and the cellular environment through the high rate of diffusion of reactive species, but also by an increased ability to solubilize chitosan in the environment of the cell culture, induced by the weak acid environment.

The osteoinductive effect on the MG-63 osteoblast cultures of the KNN content in the non-polarized composites gels and scaffolds could not be observed, through the short-term incubation (24h). To exercise the piezoelectric behavior of the composites in the HA-KNN-CS system, scaffolds and gels required external stimulation, such as electrical polarization or the application of mechanical stresses during the measurement of the antibacterial effect and cell viability. The polarization procedures of dense materials could not be applied in the case of porous composite scaffolds, and the application of mechanical stresses on them would have led to the destruction of the designed scaffolds porous texture. In addition, these methods do not simulate physiological conditions. However, the non-toxic effect of

the solid solution (biocompatibility) was evaluated both as a powder and in the form of composite scaffolds and gels.

CONCLUSIONS

From chapters I and II of the general Part I "The critical analysis of the current state of research", it was concluded that in current dental practice, one of the requirements for new generation bone addition materials should fulfill the ability to reduce the duration of *de novo* bone restoration. This requirement cannot be achieved by using biomaterials with mimetic compositions with bone tissue, in which case physiologically restoration of the tissue may require between 6 weeks and 2 months. By purchasing biocompatible components that induce the acceleration of some biological processes, such as piezoelectric ones, the repairment duration can be reduced. At the level of the oral cavity, especially during mastication, the mechanical stresses, achieved through the dentition, are transmitted to the bone tissue of the dental alveoli, thus regulating the processes related to bone restructuring. In the absence of the appropriate dentition and the exogenous pressure stimulus, in the affected areas, the alveolar bone will resorb physiologically.

Thus, three compositions in the HA-KNN-CS system were chosen, that were prepared by embedding the powders in the chitosan hydrogels, varying the mass ratio between the two HA and KNN powders (90/10, 10/90 and 50/50) keeping the content constant of 30% chitosan. The synthesis of HA, KNN and CS components aimed at obtaining the compound with the best properties, each of the components bringing their own but synergistic contributions to the functional properties of the composite. In the synthesis of HA with eggshell as a source, from the five variants obtained, following the characterization, it was decided to use variant HA 1 with nanometer-sized particles with the morphology of mesoporous bars, obtained by co-precipitation and hydrothermal maturation at 200°C, after a full cycle of 60 minutes. It demonstrated the best biocompatibility against the MC3T3 osteoblast cell line compared to the other four samples, better cell viability compared to Bio-Oss bovine bone granules and generating less oxidative stress than the xenografts with which it was compared. Among the three variants of chitosan hydrogels tested, the best results in terms of antibacterial and antifungal properties as well as inducing good viability towards MG-63 type osteoblasts compared to the CTRL sample had the chitosan with low molecular mass and medium degree of deacetylation solubilized in aqueous solution of 1.5% glacial acetic acid. Among the 15 samples of KNN, with the highest values of the piezoelectric coefficient d33 ~ 1.2pC/N, we find it in the specimen K0.47Na0.53NbO3, having submicron grains with cuboidal morphology, obtained by maturing in hydrothermal conditions at 250°C at the duration of the landing is 30 minutes. It showed biocompatibility comparable to that of the HA sample when testing the viability of MG-63 osteoblast cells by the MTT method.

The morpho-structural characteristics of the three compositions 10HA-90KNN-CSL1.5, 50HA-50KNN-CSL1.5, and 90HA-10KNN-CSL1.5 were similar, but the composite sample with a high content of piezoelectric powder (10HA-90KNN -CSL1.5) demonstrated superior antibacterial properties against *S. aureus* and *E. coli* and antifungal against *C. albicans* than the version with 90% HA, even in the absence of prior polarization or external electrical stimulation of the gels and a weaker effect of all scaffold

compositions form. Also, the viability of MG-63 osteoblast cells in contact with gels samples 10HA-90KNN-$CSL_{1.5}$ and 90HA-10KNN-$CSL_{1.5}$ showed close values of reductase secretion comparable to the CTRL sample, and lower values at scaffolds, according to the MTT test method.

FUTURE RESEARCH PERSPECTIVES

Research perspectives can be framed into two directions:

- Establishing the *in vitro* behavior for the compositions already synthesized in the HA-KNN-$CSL_{1.5}$ system
  - Establishing a method of polarization of porous composite scaffolds synthesized by lyophilization to enhance the piezoelectric effect and determine the improvements brought by the KNN component,
  - establishing the *in vitro* antibacterial behavior and cell viability of the lyophilized scaffolds after polarization or under the conditions of application of external microelectrical stimuli, then testing the ATP-ase secretion activity (through the luciferase content) by the osteoblast cell cultures in contact with the polarized scaffolds (GSH Test)
  - tracking the *in vitro* behavior of the freeze-dried scaffolds after stimulation with LIPUS (Low Intensity Pulsed Ultrasound) devices, non-invasive technology that uses the pulse frequency of 1.5 MHz with the width of 200 μs, with the spotting frequency of 1kHz.
  - *In vivo* testing of synthesized biomaterials
- SPS sintering of dense KNN scaffolds coupled with them coating with chitosan- HA gel suspension by 3D printing method and testing the behavior *in vitro* and *in vivo*.

SELECTIVE REFERENCES

[1] J. Botelho, V. Machado, Y. Leira, L. Proenca, L. Chambrone, J.J. Mendes, Economic burden of periodontitis in the United States and Europe: An updated estimation, J Periodontol, 93 (2022) 373-379.
[2] G. Iviglia, S. Kargozar, F. Baino, Biomaterials, Current Strategies, and Novel Nano-Technological Approaches for Periodontal Regeneration, J Funct Biomater, 10 (2019).
[3] Y. Lee, Association between osteoporosis and periodontal disease among menopausal women: The 2013-2015 Korea National Health and Nutrition Examination Survey, PLoS One, 17 (2022) e0265631.
[4] S. Titsinides, G. Agrogiannis, T. Karatzas, Bone grafting materials in dentoalveolar reconstruction: A comprehensive review, Jpn Dent Sci Rev, 55 (2019) 26-32.
[5] M. Khanijou, D. Seriwatanachai, K. Boonsiriseth, S. Suphangul, V. Pairuchvej, R.L. Srisatjaluk, N. Wongsirichat, Bone graft material derived from extracted tooth: A review literature, Journal of Oral and Maxillofacial Surgery, Medicine, and Pathology, 31 (2019) 1-7.
[6] S. Prasadh, R.C.W. Wong, Unraveling the mechanical strength of biomaterials used as a bone scaffold in oral and maxillofacial defects, Oral Science International, 15 (2018) 48-55.
[7] I. Mencia Castano, Curtin, C. M.Duffy, G. P. O'Brien, F. J., Next generation bone tissue engineering: non-viral miR-133a inhibition using collagen-nanohydroxyapatite scaffolds rapidly enhances osteogenesis, Sci Rep, 6 (2016) 27941.

[8] S. Kuroshima, M. Kaku, T. Ishimoto, M. Sasaki, T. Nakano, T. Sawase, A paradigm shift for bone quality in dentistry: A literature review, J Prosthodont Res, 61 (2017) 353-362.
[9] J.G. Caton, G. Armitage, T. Berglundh, I.L.C. Chapple, S. Jepsen, K.S. Kornman, B.L. Mealey, P.N. Papapanou, M. Sanz, M.S. Tonetti, A new classification scheme for periodontal and peri-implant diseases and conditions - Introduction and key changes from the 1999 classification, J Clin Periodontol, 45 Suppl 20 (2018) S1-S8.
[10] W. Wang, K.W.K. Yeung, Bone grafts and biomaterials substitutes for bone defect repair: A review, Bioact Mater, 2 (2017) 224-247.
[11] G. Turnbull, J. Clarke, F. Picard, P. Riches, L. Jia, F. Han, B. Li, W. Shu, 3D bioactive composite scaffolds for bone tissue engineering, Bioact Mater, 3 (2018) 278-314.
[12] J. Venkatesan, B. Lowe, S. Anil, S.-K. Kim, M.S. Shim, Combination of Nano-Hydroxyapatite with Stem Cells for Bone Tissue Engineering, Journal of Nanoscience and Nanotechnology, 16 (2016) 8881-8894.
[13] M. Figueiredo, J. Henriques, G. Martins, F. Guerra, F. Judas, H. Figueiredo, Physicochemical characterization of biomaterials commonly used in dentistry as bone substitutes--comparison with human bone, J Biomed Mater Res B Appl Biomater, 92 (2010) 409-419.
[14] Y. Zhang, L. Chen, J. Zeng, K. Zhou, D. Zhang, Aligned porous barium titanate/hydroxyapatite composites with high piezoelectric coefficients for bone tissue engineering, Mater Sci Eng C Mater Biol Appl, 39 (2014) 143-149.
[15] Q. Xu, X. Gao, S. Zhao, Y.N. Liu, D. Zhang, K. Zhou, H. Khanbareh, W. Chen, Y. Zhang, C. Bowen, Construction of Bio-Piezoelectric Platforms: From Structures and Synthesis to Applications, Adv Mater, 33 (2021) e2008452.
[16] B.E. Cameron J. Wilson, Ricgard E. Clegg, David I. Leavesley, and Mark J. Pearcy, Mediation of Biomaterial–Cell Interactions by Adsorbed Proteins: A Review, Tissue Engineering, 11 (2005) 1-18.
[17] J. Pajarinen, T. Lin, E. Gibon, Y. Kohno, M. Maruyama, K. Nathan, L. Lu, Z. Yao, S.B. Goodman, Mesenchymal stem cell-macrophage crosstalk and bone healing, Biomaterials, 196 (2019) 80-89.
[18] J.J. El-Jawhari, E. Jones, P.V. Giannoudis, The roles of immune cells in bone healing; what we know, do not know and future perspectives, Injury, 47 (2016) 2399-2406.
[19] L.C. Gerstenfeld, D.M. Cullinane, G.L. Barnes, D.T. Graves, T.A. Einhorn, Fracture healing as a post-natal developmental process: molecular, spatial, and temporal aspects of its regulation, J Cell Biochem, 88 (2003) 873-884.
[20] G.S. Selders, A.E. Fetz, M.Z. Radic, G.L. Bowlin, An overview of the role of neutrophils in innate immunity, inflammation and host-biomaterial integration, Regen Biomater, 4 (2017) 55-68.
[21] R.C. Lai, R.W. Yeo, S.K. Lim, Mesenchymal stem cell exosomes, Semin Cell Dev Biol, 40 (2015) 82-88.
[22] S. Saidin, M.A. Jumat, N.A.A. Mohd Amin, A.S. Saleh Al-Hammadi, Organic and inorganic antibacterial approaches in combating bacterial infection for biomedical application, Mater Sci Eng C Mater Biol Appl, 118 (2021) 111382.
[23] A. Singh, A.K. Dubey, Various Biomaterials and Techniques for Improving Antibacterial Response, ACS Applied Bio Materials, 1 (2018) 3-20.
[24] P.M. Kou, J.E. Babensee, Macrophage and dendritic cell phenotypic diversity in the context of biomaterials, J Biomed Mater Res A, 96 (2011) 239-260.
[25] T.J.U. Thompson, M. Gauthier, M. Islam, The application of a new method of Fourier Transform Infrared Spectroscopy to the analysis of burned bone, Journal of Archaeological Science, 36 (2009) 910-914.
[26] B.M. Marija Kosec, Andreja Bencan, and Tadej Rojac, KNN-Based Piezoelectric Ceramics, Piezoelectric and Acoustic Materials for Transducer Applications Springer, Boston, MA2008, pp. pp 81-102.
[27] F. Rubio-Marcos, J.J. Romero, M.S. Martín-Gonzalez, J.F. Fernández, Effect of stoichiometry and milling processes in the synthesis and the piezoelectric properties of modified KNN nanoparticles by solid state reaction, Journal of the European Ceramic Society, 30 (2010) 2763-2771.
[28] Y. Inagaki, K.-i. Kakimoto, I. Kagomiya, Ferroelectric Domain Characterization of Orthorhombic Sodium-Potassium Niobate Piezoelectric Crystals, Journal of the American Ceramic Society, 93 (2010) 4061-4065.

[29] S. Kojima, J. Zushi, Y. Noguchi, M. Miyayama, Successive phase transition of lead-free ferroelectric sodium potassium niobate crystals studied by Raman scattering, Ferroelectrics, 532 (2019) 183-189.
[30] J. Xing, L. Jiang, C. Zhao, Z. Tan, Q. Xu, J. Wu, Q. Chen, D. Xiao, J. Zhu, Potassium sodium niobate based lead-free ceramic for high-frequency ultrasound transducer applications, Journal of Materiomics, 6 (2020) 513-522.
[31] Y. Ito, A. Tateyama, Y. Nakamura, T. Shimizu, M. Kurosawa, H. Uchida, T. Shiraishi, T. Kiguchi, T.J. Konno, M. Ishikawa, N. Kumada, H. Funakubo, High yield preparation of (100)c-oriented (K,Na)NbO3 thick films by hydrothermal method using amorphous niobium source, Journal of the Ceramic Society of Japan, 128 (2020) 512-517.
[32] J. BARCLAY, Injection of acetyc acid in cancer, British Medical Journal, (1866).
[33] C. Gupta, A. Agrawal, N.D. Gargav, Role of Acetic Acid Irrigation in Medical Management of Chronic Suppurative Otitis Media: A Comparative Study, Indian J Otolaryngol Head Neck Surg, 67 (2015) 314-318.
[34] X.S. Shaojie Lu, Deyong Cao, Yiping Chen, Kangde Yao, Preparation of Water-Soluble Chitosan, Journal of Applied Polymer Science, 91 (2004) 3497–3503.
[35] M. Ioelovich, Crystallinity and Hydrophility of Chitin and Chitosan, RRJC Volume 3 (2014).
[36] T. Yao, J. Chen, Z. Wang, J. Zhai, Y. Li, J. Xing, S. Hu, G. Tan, S. Qi, Y. Chang, P. Yu, C. Ning, The antibacterial effect of potassium-sodium niobate ceramics based on controlling piezoelectric properties, Colloids Surf B Biointerfaces, 175 (2019) 463-468.
[37] G. Tan, S. Wang, Y. Zhu, L. Zhou, P. Yu, X. Wang, T. He, J. Chen, C. Mao, C. Ning, Surface-Selective Preferential Production of Reactive Oxygen Species on Piezoelectric Ceramics for Bacterial Killing, ACS Appl Mater Interfaces, 8 (2016) 24306-24309.
[38] A.S. Verma, A. Singh, D. Kumar, A.K. Dubey, Electro-mechanical and Polarization-Induced Antibacterial Response of 45S5 Bioglass-Sodium Potassium Niobate Piezoelectric Ceramic Composites, ACS Biomater Sci Eng, 6 (2020) 3055-3069.
[39] P. Agalya, G. Suresh Kumar, R. Srinivasan, K.M. Prabu, G. Karunakaran, S. Cholan, E. Kolesnikov, M. Kim, Hydroxyapatite-based antibacterial bio-nanomaterials: an insight into the synthesis using mussel shell as a calcium source, physicochemical properties, and nanoindentation characteristics, Applied Physics A, 127 (2021).